Recent advances in monoclinic crystal optics

Yannick Petit, Simon Joly, Patricia Segonds, Benoit Boulanger

LASER & PHOTONICS REVIEWS

Laser Photonics Rev. (2013) / **DOI** 10.1002/lpor.XXXXXXXXXX

Abstract This article is mainly devoted to the modeling and measurement of the absorption and fluorescence angular distributions in polarized light of monoclinic crystals. Up to now theoretical crystal optics were mostly devoted to crystals having a high crystallographic symmetry. In these crystals belonging to the cubic, hexagonal, tetragonal, trigonal or orthorhombic lattice classes, the tensor properties related to the real part of the dielectric permittivity and to its imaginary part can be described in the same frame which orientation does not vary as a function of wavelength. The situation is much more complicated in the case of monoclinic crystals because it is necessary to define a specific frame for each property and each wavelength that are considered. The main features of monoclinic crystal optics are described in detail, followed by a review of monoclinic materials and the consequence of these features on their related optical properties.

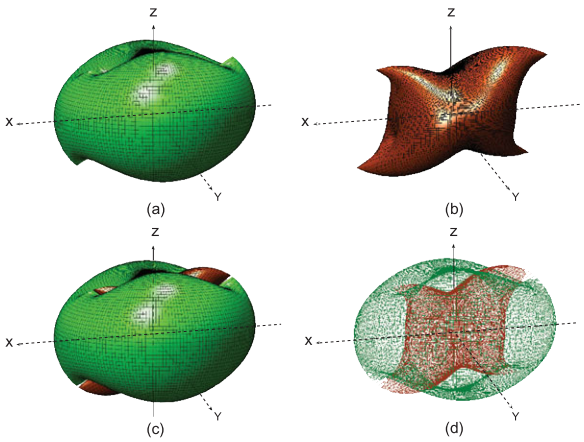

Recent advances in monoclinic crystal optics

Yannick Petit[1,2], Simon Joly[3], Patricia Segonds[4], and Benoît Boulanger[4,*]

1. Introduction

An increasing number of crystals belonging to the three monoclinic point groups, i.e. *2*, *m*, *2/m* where *2* stands for a two-fold axis and *m* for a mirror plane [1], are identified as promising materials for numerous optical properties and applications such as laser emission [2], nonlinear frequency conversion [3], self-doubling [4], scintillation [5], photorefractivity [6], quantum memories and slow light [7] for example. Monoclinic crystals belong to the biaxial optical class, which means that they have three principal refractive indices, n_x, n_y and n_z where x, y and z refer to the dielectric axes, exhibiting different magnitudes [8]. Contrary to the three orthorhombic crystals *222*, *mm2* and *mmm* that are the biaxial crystals of highest crystallographic symmetry, the crystallographic axes of monoclinic crystals do not coincide with the dielectric frame that is defined as the frame where the real part of the complex dielectric permittivity tensor is diagonal [8]. It is a first level of difficulty for the use of monoclinic crystals since the orientation of the dielectric frame may vary as a function of any dispersive parameters of the refractive index as the wavelength or the temperature for example, while the crystallographic frame orientation remains unchanged [9]. Then the ability to characterize and exploit at best these low symmetry crystals requires to properly master not only the real part of the dielectric permittivity but also the imaginary part. Even if numerous theoretical treatments of crystal optics including absorbing media of any symmetry has been performed from the 19th century to the beginning of the 20th century [10], there have been very few experiments devoted to the investigation of the imaginary part of monoclinic crystals. The present review article aims at updating the state of the art of monoclinic crystal optics from several theoretical and experimental studies devoted to the anisotropy of the imaginary part of the linear dielectric permittivity, including absorption as well as fluorescence [11–17]. Actually unexpected features were discovered, like the necessity to define new physical frames, the so-called absorption or fluorescence frames, whose principal axes afford to diagonalize the imaginary part of the dielectric permittivity tensor and to measure the corresponding eigenvalues. Furthermore, the relative orientation between the dielectric, absorption and fluorescence frames strongly depends on the considered electronic transition. Another interesting property is the existence of a continuum of directions of propagation exhibiting a polarization-independent behaviour for the magnitude of absorption or fluorescence. All these features related to the imaginary part of the dielectric permittivity undoubtedly constitute a significant step of difficulty for the design of optical devices based on monoclinic crystals. This fundamental review also includes a description of suited methodologies for accurately characterizing monoclinic crystals, a review of the main monoclinic materials

[1] CNRS, ICMCB, UPR 9048, F-33608 Pessac, France
[2] Univ. Bordeaux, ICMCB, UPR 9048, F-33400 Pessac, France
[3] CEA Leti-MINATEC, 17 rue des Martyrs, 38054 Grenoble Cedex 9, France
[4] Institut Néel CNRS Université Joseph Fourier, 25 rue des Martyrs, BP 166, F38402 Grenoble Cedex 9, France
*Corresponding author(s): e-mail: benoit.boulanger@Grenoble.cnrs.fr

as well as their related optical properties, and opens new research fields devoted to laser and nonlinear optics, as well as scintillation science or photorefractivity.

2. Dielectric permittivity

2.1. Tensorial formalism of the complex dielectric permittivity

This part provides the main theoretical background used in the article. We consider electromagnetic waves with a wavelength λ ranging typically from the deep Ultra-Violet (10 nm) to the far Infrared (100 μm). We are interested in homogenous dielectric media with no electric conductivity or free charges, and without magnetic properties. Then we focus on the electric field of light, its propagation being described by Maxwell's equations. We also restrict to media with large dimensions compared to wavelength so that the propagation is not affected by diffraction or guiding effects.

We assume sinusoidal monochromatic plane waves for describing each Fourier component $\vec{E}(\omega)$ of the light at the circular frequency ω. Given the previous range of wavelengths, the light-matter interaction induces a deformation of the valence electron density. We will restrict the electronic response to dipolar response and the corresponding dipole moment is labeled at the macroscopic scale as the polarization of the medium and written $\vec{P}(\omega)$. In the weak coupling regime, this polarization is directly proportional to the excitation light electric field vector, which defines the constitutive equation of the light-matter interaction in the linear regime, i.e. [18]:

$$\vec{P}(\omega) = \varepsilon_0 \overline{\overline{\hat{\chi}}}^{(1)}(\omega).\vec{E}(\omega) \tag{1}$$

$\varepsilon_0 = (36\pi 10^9)^{-1}$ F/m is the dielectric permittivity of the vacuum, $\vec{E}(\omega) = \vec{e}(\omega)E(\omega)$ is the electric field of the excitation light at the circular frequency ω, where $\vec{e}(\omega)$ is the unit vector and $E(\omega)$ is the complex amplitude; the dot stands for a contraction product, and the first order electric susceptibility $\overline{\overline{\hat{\chi}}}^{(1)}(\omega)$ is a second rank polar tensor that writes in any frame as a 3×3 matrix. Due to possible losses in the medium, $\overline{\overline{\hat{\chi}}}^{(1)}(\omega)$ is a complex tensor which real and imaginary parts are labeled as $\overline{\overline{\chi}}^{(1)}(\omega)$ and $\overline{\overline{\chi'}}^{(1)}(\omega)$ respectively. Then it comes:

$$\overline{\overline{\hat{\chi}}}^{(1)}(\omega) = \overline{\overline{\chi}}^{(1)}(\omega) + j\overline{\overline{\chi'}}^{(1)}(\omega) \tag{2}$$

Note that the spectra resulting from the real and imaginary parts are linked by the Kramers-Krönig relations [19]. For propagation purpose, it is useful to consider the electric displacement $\vec{D}(\omega)$ defined as $\vec{D}(\omega) = \vec{P}(\omega) + \varepsilon_0\vec{E}(\omega)$; thus according to Eq. (1) it is written:

$$\vec{D}(\omega) = \varepsilon_0[1 + \overline{\overline{\hat{\chi}}}^{(1)}(\omega)].\vec{E}(\omega) = \varepsilon_0\overline{\overline{\hat{\varepsilon}_r}}(\omega).\vec{E}(\omega) \tag{3}$$

where $\overline{\overline{\hat{\varepsilon}_r}}(\omega)$ is the relative dielectric permittivity tensor of the medium written as following according to Eq. (2):

$$\overline{\overline{\hat{\varepsilon}_r}}(\omega) = \overline{\overline{\varepsilon_r}}(\omega) + j\overline{\overline{\varepsilon'_r}}(\omega) \tag{4}$$

$\overline{\overline{\varepsilon_r}}(\omega)$ is the real part of the relative dielectric permittivity governing the propagation and the refractive index, while $\overline{\overline{\varepsilon'_r}}(\omega)$ is the imaginary part related to absorption as well as fluorescence [12]. The general matrix writing of Eq. (4) in a direct tri-rectangular frame *(u, v, w)* is:

$$\overline{\overline{\hat{\varepsilon}_r}} = \begin{bmatrix} \hat{\varepsilon}_{r_{uu}} & \hat{\varepsilon}_{r_{uv}} & \hat{\varepsilon}_{r_{uw}} \\ \hat{\varepsilon}_{r_{vu}} & \hat{\varepsilon}_{r_{vv}} & \hat{\varepsilon}_{r_{vw}} \\ \hat{\varepsilon}_{r_{wu}} & \hat{\varepsilon}_{r_{wv}} & \hat{\varepsilon}_{r_{ww}} \end{bmatrix} = \begin{bmatrix} \varepsilon_{r_{uu}} & \varepsilon_{r_{uv}} & \varepsilon_{r_{uw}} \\ \varepsilon_{r_{vu}} & \varepsilon_{r_{vv}} & \varepsilon_{r_{vw}} \\ \varepsilon_{r_{wu}} & \varepsilon_{r_{wv}} & \varepsilon_{r_{ww}} \end{bmatrix} + j \begin{bmatrix} \varepsilon'_{r_{uu}} & \varepsilon'_{r_{uv}} & \varepsilon'_{r_{uw}} \\ \varepsilon'_{r_{vu}} & \varepsilon'_{r_{vv}} & \varepsilon'_{r_{vw}} \\ \varepsilon'_{r_{wu}} & \varepsilon'_{r_{wv}} & \varepsilon'_{r_{ww}} \end{bmatrix} \tag{5}$$

The number of independent tensor coefficients and the relationships between them can be found using the Neumann principle, which stipulates that a tensor describing any physical property of a given medium has to remain invariant with respect to all the symmetry elements of this medium [8]. As a consequence, it can be shown that $\varepsilon_{r_{ij}} = \varepsilon_{r_{ji}}$ and $\varepsilon'_{r_{ij}} = \varepsilon'_{r_{ji}}$, where $(i, j) = (u, v \text{ or } w)$, for all the possible lattice point groups: cubic, hexagonal, tetragonal, trigonal, orthorhombic, monoclinic and triclinic [1]. Furthermore, some tensor coefficients of Eq. (5) can be nil. In the case of the three point groups of the monoclinic system, i.e. *2*, *m and 2/m*, and by considering as an example that the *v*-axis of the (*u*, *v*, *w*) frame is perpendicular to the mirror *m* or parallel to the two-fold axis *2* we get: $\varepsilon_{r_{uv}} = \varepsilon_{r_{vu}} = \varepsilon_{r_{vw}} = \varepsilon_{r_{wv}} = 0$ and $\varepsilon'_{r_{uv}} = \varepsilon'_{r_{vu}} = \varepsilon'_{r_{vw}} = \varepsilon'_{r_{wv}} = 0$. Finally the application of the Neumann principle enables to state that the five remaining non-zero coefficients verify: $\varepsilon_{r_{uu}} + j\varepsilon'_{r_{uu}} \neq \varepsilon_{r_{vv}} + j\varepsilon'_{r_{vv}} \neq \varepsilon_{r_{ww}} + j\varepsilon'_{r_{ww}} \neq \varepsilon_{r_{uw}} + j\varepsilon'_{r_{uw}} = \varepsilon_{r_{wu}} + j\varepsilon'_{r_{wu}}$. The two other conventions for the relationships between the dielectric frame and the symmetry elements, i.e. the *u*-axis or *w*-axis perpendicular to the mirror *m* or parallel to the two-fold axis *2*, are less common but may be used, which gives the respective non-zero coefficients: $\varepsilon_{r_{uu}} + j\varepsilon'_{r_{uu}} \neq \varepsilon_{r_{vv}} + j\varepsilon'_{r_{vv}} \neq \varepsilon_{r_{ww}} + j\varepsilon'_{r_{ww}} \neq \varepsilon_{r_{vw}} + j\varepsilon'_{r_{vw}} = \varepsilon_{r_{wv}} + j\varepsilon'_{r_{wv}}$ for the *u*-axis case; and $\varepsilon_{r_{uu}} + j\varepsilon'_{r_{uu}} \neq \varepsilon_{r_{vv}} + j\varepsilon'_{r_{vv}} \neq \varepsilon_{r_{ww}} + j\varepsilon'_{r_{ww}} \neq \varepsilon_{r_{uv}} + j\varepsilon'_{r_{uv}} = \varepsilon_{r_{vu}} + j\varepsilon'_{r_{vu}}$ for the *w*-axis case.

2.2. Principal frames associated with the real and imaginary parts of the relative dielectric permittivity

When expressed in their respective proper tri-rectangular frames, the tensors of Eq. (5) write as matrices with only diagonal coefficients that are the three main values of the considered tensor. This particular frame for the real part

$\overline{\overline{\varepsilon_r}}(\omega)$ is the so-called dielectric frame written (x, y, z). However there is no physical reason that imposes the dielectric frame to be also the principal frame of the imaginary part $\overline{\overline{\varepsilon'_r}}(\omega)$. Then in the dielectric frame, the most general writing of Eq. (5) in the case of a monoclinic crystal where the y-axis is perpendicular to the mirror m or parallel to the two-fold axis *2* is the following [13]:

$$\overline{\overline{\hat{\varepsilon}_r}} = \begin{bmatrix} \hat{\varepsilon}_{r_{xx}} & 0 & \hat{\varepsilon}_{r_{xz}} \\ 0 & \hat{\varepsilon}_{r_{yy}} & 0 \\ \hat{\varepsilon}_{r_{xz}} & 0 & \hat{\varepsilon}_{r_{zz}} \end{bmatrix} = \begin{bmatrix} \varepsilon_{r_{xx}} & 0 & 0 \\ 0 & \varepsilon_{r_{yy}} & 0 \\ 0 & 0 & \varepsilon_{r_{zz}} \end{bmatrix} + j \begin{bmatrix} \varepsilon'_{r_{xx}} & 0 & \varepsilon'_{r_{xz}} \\ 0 & \varepsilon'_{r_{yy}} & 0 \\ \varepsilon'_{r_{xz}} & 0 & \varepsilon'_{r_{zz}} \end{bmatrix} \tag{6}$$

It can be then useful to introduce and define the specific principal frame of $\overline{\overline{\varepsilon'_r}}(\omega)$, which we called the absorption or fluorescence frame according to which property is considered, written (x', y', z') [13]. Thus in this frame, the imaginary relative dielectric permittivity tensor becomes diagonal, i.e.:

$$\overline{\overline{\varepsilon'_r}} = \begin{bmatrix} \varepsilon'_{r_{xx}} & 0 & \varepsilon'_{r_{xz}} \\ 0 & \varepsilon'_{r_{yy}} & 0 \\ \varepsilon'_{r_{xz}} & 0 & \varepsilon'_{r_{zz}} \end{bmatrix} = \begin{bmatrix} \varepsilon'_{r_{x'x'}} & 0 & 0 \\ 0 & \varepsilon'_{r_{y'y'}} & 0 \\ 0 & 0 & \varepsilon'_{r_{z'z'}} \end{bmatrix} \tag{7}$$

with $\varepsilon'_{r_{x'x'}} \neq \varepsilon'_{r_{y'y'}} \neq \varepsilon'_{r_{z'z'}}$ according to the symmetry considerations developed in section 2.1. Note that four independent elements are required to express $\overline{\overline{\varepsilon'_r}}(\omega)$ in the dielectric frame, while only three are necessary in the imaginary eigenframe. In the latter frame, the fourth independent information is then no more a tensor element, but the angle between the orientation of the dielectric and imaginary frames, as it will be discussed in section 3.3. Even if the present paper is exclusively devoted to the high frequency linear response of matter, i.e. the linear electric susceptibility at optical frequencies, it is important to indicate that for monoclinic crystals the low-frequency (static) electric susceptibility is defined in its own frame that does not coincide with the "optical dielectric frame" as it will be shown in section 6.5.

3. Optical angular distributions

3.1. Propagation equation

Light-matter interactions for linear electric dipolar processes are well described in the dielectric frame using sinusoidal monochromatic plane waves and the following propagation equation in the linear regime [12, 14]:

$$\hat{n}^2(\omega, \theta, \varphi)[\vec{u}(\theta, \varphi) \times (\vec{u}(\theta, \varphi) \times \vec{E}(\omega, \theta, \varphi))] + \overline{\overline{\hat{\varepsilon}_r}}(\omega)\vec{E}(\omega, \theta, \varphi) = 0 \tag{8}$$

$\overline{\overline{\hat{\varepsilon}_r}}(\omega)$ is the linear relative dielectric permittivity defined by Eqs. (4) and (5); $\times$ is the vectorial product; $\vec{E}(\omega, \theta, \varphi)$ is the light electric field at the circular frequency ω depending on (θ, φ) that are the angles of spherical coordinates in the dielectric frame (x, y, z) of the unit vector $\vec{u}(\theta, \varphi)$ of the wave vector $\vec{k}(\omega, \theta, \varphi) = \omega c^{-1}\hat{n}(\omega, \theta, \varphi)\vec{u}(\theta, \varphi)$, where c is the light velocity in vacuum and $\hat{n}(\omega, \theta, \varphi)$ is the complex optical index defined by:

$$\hat{n}(\omega, \theta, \varphi) = n(\omega, \theta, \varphi) + jn'(\omega, \theta, \varphi) \tag{9}$$

The real part n is the refractive index while the imaginary part n' governs absorption or fluorescence i.e. [12]:

$$\xi(\omega, \theta, \varphi) = 2\omega c^{-1} n'(\omega, \theta, \varphi) \tag{10}$$

ξ [cm^{-1}] can be the absorption or fluorescence coefficient according to the phenomenon that is considered during the light propagation. As it appears in the notations above, the real and imaginary parts of the optical index depend on the circular frequency, which is well described by the classical Lorentz model [12].

In monoclinic crystals $\overline{\overline{\hat{\varepsilon}_r}}(\omega)$ is given by Eq. (6). The projection of Eq. (8) on the three principal axes of the dielectric frame leads to the following linear system of three coupled equations at the circular frequency ω in the considered direction of the wave vector (θ, φ):

$$\begin{cases} \left[\hat{\varepsilon}_{r_{xx}} - \hat{n}^2\left(u_y^2 + u_z^2\right)\right]E_x + \left[\hat{\varepsilon}_{r_{xy}} + \hat{n}^2 u_x u_y\right]E_y \\ \qquad + \left[\hat{\varepsilon}_{r_{xz}} + \hat{n}^2 u_x u_z\right]E_z = 0 \\ \left[\hat{\varepsilon}_{r_{yx}} + \hat{n}^2 u_y u_x\right]E_x + \left[\hat{\varepsilon}_{r_{yy}} - \hat{n}^2\left(u_x^2 + u_z^2\right)\right]E_y \\ \qquad + \left[\hat{\varepsilon}_{r_{yz}} + \hat{n}^2 u_y u_z\right]E_z = 0 \\ \left[\hat{\varepsilon}_{r_{zx}} + \hat{n}^2 u_z u_x\right]E_x + \left[\hat{\varepsilon}_{r_{zy}} + \hat{n}^2 u_z u_y\right]E_y \\ \qquad + \left[\hat{\varepsilon}_{r_{zz}} - \hat{n}^2\left(u_x^2 + u_y^2\right)\right]E_z = 0 \end{cases} \tag{11}$$

(E_x, E_y, E_z) and (u_x, u_y, u_z) are the Cartesian coordinates of the electric field vector and of the unit wave vector respectively. Then $u_x = \sin\theta\cos\varphi$, $u_y = \sin\theta\sin\varphi$ and $u_z = \cos\theta$. Note that the circular frequency ω does not appear in Eq. (11) for more clarity. The same omission will be used in the following.

The calculation of the determinant of the linear system (11) leads to the determination of two possible non trivial complex solutions, giving way for the real part of the optical index to two real solutions, written $n^+(\theta, \varphi)$ and $n^-(\theta, \varphi)$ on the one hand, and to two possible values for the imaginary part, $n'^+(\theta, \varphi)$ and $n'^-(\theta, \varphi)$, on the other hand.

The two sets of solutions $(n^+(\theta, \varphi), n'^+(\theta, \varphi))$ and $(n^-(\theta, \varphi), n'^-(\theta, \varphi))$ are respectively associated with two different electric fields $\vec{E}^+(\theta, \varphi)$ and $\vec{E}^-(\theta, \varphi)$ in the considered direction of propagation (θ, φ). Under the weak absorption or fluorescence approximation, i.e. $n'^{\pm}(\theta, \varphi) \ll n^{\pm}(\theta, \varphi)$, which corresponds to n'/n of the order of 10^{-4}, the unit vectors of the two electric fields only depend on the

real part of the optical index [20, 21], and they are defined by the following relation according to Eq. (11):

$$e_i^{\pm}(\theta,\varphi) = \frac{n^{\pm}(\theta,\varphi)^2}{\left(n^{\pm}(\theta,\varphi)^2 - n_i^2\right)} u_i(\theta,\varphi)[\vec{u}(\theta,\varphi).\vec{e}^{\pm}(\theta,\varphi)] \tag{12}$$

where $n_i^2 = \varepsilon_{r_{ii}}$ stands for the square of principal refractive indices with $i = x, y$ or z. These two polarization eigenmodes unit vectors define the neutral lines associated with the direction of propagation that is considered [8]. They are orthogonal one to each other only in the principal planes xy, xz and yz of the dielectric frame where they are called the "ordinary" and "extraordinary" electric fields vectors. This specific denomination is not relevant outside the principal planes of biaxial crystals where the denomination (+) and (-) has to be used [21].

3.2. Angular distribution of the real part of the optical index

The angular distribution of the real part of the optical index $n^{\pm}(\theta,\varphi)$ can be obtained from the numerical resolution of the real part of Eq. (11) as well as from the analytical resolution of the lossless Fresnel equation [22] in the dielectric frame (x, y, z) leading to the well-known double-layer index surface:

$$n^{\pm}(\theta,\varphi) = \left[\frac{2}{-B \mp (B^2 - 4C)^{1/2}}\right]^{1/2} \tag{13}$$

with $B = -u_x^2(b+c) - u_y^2(a+c) - u_z^2(a+b)$, $C = u_x^2 bc + u_y^2 ac + u_z^2 ab$; $a = \varepsilon_{r_{xx}}^{-1} = n_x^{-2}$, $b = \varepsilon_{r_{yy}}^{-1} = n_y^{-2}$ and $c = \varepsilon_{r_{zz}}^{-1} = n_z^{-2}$. Equation (13) is not only valid for monoclinic crystals but also for any other biaxial crystal belonging to the orthorhombic and triclinic point groups.

The section of the index surface in each of the principal planes xy, yz and xz is given below in terms of ordinary refractive index $n_{uv}^o(\theta,\varphi)$ and extraordinary refractive index $n_{uv}^e(\theta,\varphi)$, where uv stands for the planes xy, yz or xz [12]:

$$\begin{aligned}
n_{xy}^e(\varphi) &= n_z \ \text{ and } \ n_{xy}^o(\varphi) = \left(\frac{\cos^2(\varphi)}{n_y^2} + \frac{\sin^2(\varphi)}{n_x^2}\right)^{-1/2} \\
n_{yz}^o(\theta) &= n_x \ \text{ and } \ n_{yz}^e(\theta) = \left(\frac{\cos^2(\theta)}{n_y^2} + \frac{\sin^2(\theta)}{n_z^2}\right)^{-1/2} \\
n_{xz}^o(\theta) &= n_y \ \text{ and } \ n_{xz}^e(\theta) = \left(\frac{\cos^2(\theta)}{n_x^2} + \frac{\sin^2(\theta)}{n_z^2}\right)^{-1/2}
\end{aligned} \tag{14}$$

Equations (14) show that the ordinary section of the index surface is a circle in the yz and xz planes while it is an ellipse in the xy plane. It is the reverse situation for the extraordinary section. The xz principal plane is of specific interest because it contains four directions corresponding by pairs to two axes along which the ordinary and extraordinary refractive indices have the same magnitude. These so-called "optical axes of wave normal" (OA) define the umbilici of the index surface making an angle $V_z = \text{asin}[(n_x^{-2} - n_y^{-2})^{1/2}(n_x^{-2} - n_z^{-2})^{-1/2}]$ with the z-axis [12, 23]. The angle V_z obviously depends on the circular frequency. In this particular plane when $-V_z < \theta < V_z$ and $\pi - V_z < \theta < \pi + V_z$, then $(\vec{e}_{xz}^{\,o}(\theta), n_{xz}^o(\theta))$ and $(\vec{e}_{xz}^{\,e}(\theta), n_{xz}^e(\theta))$ correspond to $(\vec{e}_{xz}^{\,+}(\theta), n_{xz}^+(\theta))$ and $(\vec{e}_{xz}^{\,-}(\theta), n_{xz}^-(\theta))$ respectively, while at other angles the correspondence between (o, e) and (+, -) is the reverse; it means that there is a discontinuity of the direction of polarization of $\pi/2$ from either side of each optical axis of wave normal [24]. In the xy plane, $(\vec{e}_{xy}^{\,e}(\varphi), n_{xy}^e(\varphi))$ and $(\vec{e}_{xy}^{\,o}(\varphi), n_{xy}^o(\varphi))$ correspond to $(\vec{e}_{xy}^{\,+}(\varphi), n_{xy}^+(\varphi))$ and $(\vec{e}_{xy}^{\,-}(\varphi), n_{xy}^-(\varphi))$ respectively. In the yz plane, $(\vec{e}_{yz}^{\,o}(\theta), n_{yz}^o(\theta))$ and $(\vec{e}_{yz}^{\,e}(\theta), n_{yz}^e(\theta))$ correspond to $(\vec{e}_{yz}^{\,-}(\theta), n_{yz}^-(\theta))$ and $(\vec{e}_{yz}^{\,+}(\theta), n_{yz}^+(\theta))$ respectively. Note that $\vec{e}_{xz}^{\,o}(\theta)$, $\vec{e}_{xy}^{\,o}(\varphi)$ and $\vec{e}_{yz}^{\,o}(\theta)$ are all contained in the xy plane and thus are perpendicular with the optical axes, the extraordinary unit electric field vectors $\vec{e}_{xz}^{\,e}(\theta)$, $\vec{e}_{xy}^{\,e}(\varphi)$ and $\vec{e}_{yz}^{\,e}(\theta)$ being perpendicular with the corresponding ordinary ones.

The sections of the index surface in the three principal planes of the dielectric frame and the corresponding electric field vectors configurations are drawn in Fig. 1(a). Figure 1(b) gives the index surface plotted over one fourth of the space. It is important to notice that in the general case of monoclinic crystals the dielectric axes are not necessarily pinned to a crystallographic plane according to the fact that the dielectric frame is not fully linked to the crystallographic frame and that the dielectric principal plane xz may not coincide to one of the principal planes of the crystallographic frame. Note that outside the principal planes the two eigenmodes of polarization are not orthogonal according to Eq. (12).

3.3. Angular distribution of the imaginary part of the optical index

We can keep the denomination of "ordinary" and "extraordinary" for the imaginary optical index corresponding to propagations in the principal planes of the dielectric frame, which are then written $n'^o(\theta,\phi)$ and $n'^e(\theta,\phi)$ respectively. In these planes, the analytical calculations under the weak absorption or fluorescence approximations, that is to say by neglecting any square power terms of $\overline{\overline{\varepsilon'_r}}$ when expressing the condition of nullity of the determinant of Eq. (11), lead to the following expressions:

$$\begin{aligned}
n'^e_{xy}(\varphi) &= \frac{\varepsilon'_{r_{zz}}}{2n_z} \quad \text{and} \quad n'^o_{xy}(\varphi) = n_{xy}^o(\varphi)^3 \\
&\times \left[\frac{\varepsilon'_{r_{yy}}\cos^2(\varphi)}{2n_y^4} + \frac{\varepsilon'_{r_{xx}}\sin^2(\varphi)}{2n_x^4} - \frac{\varepsilon'_{r_{xy}}\sin(\varphi)\cos(\varphi)}{n_x^2 n_y^2}\right]
\end{aligned}$$

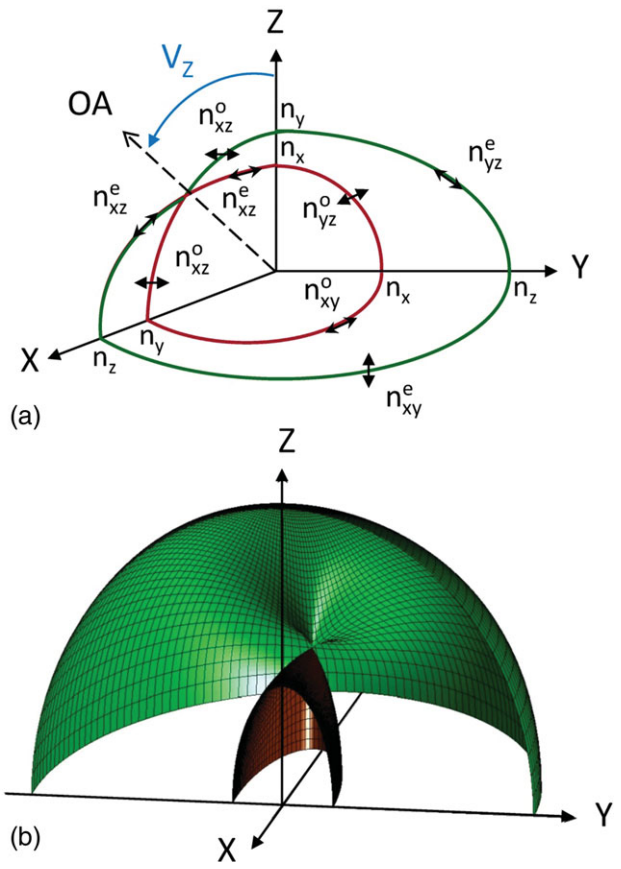

Figure 1 (online color at: www.lpr-journal.org) Index surface of a biaxial crystal (orthorhombic, monoclinic or triclinic). (a) Section in the three principal planes where the indices (o) and (e) denote the ordinary and extraordinary refractive indices respectively; OA is the optical axis of internal conical refraction in the considered octant of the space; the double arrows stand for the ordinary and extraordinary electric fields directions. (b) Schematic view from inside where the deformation of the two layers of the index surface around its umbilici clearly appears.

$$n'^{o}_{yz}(\theta) = \frac{\varepsilon'_{r_{xx}}}{2n_x} \quad \text{and} \quad n'^{e}_{yz}(\theta) = n^{e}_{yz}(\theta)^3 \times \left[\frac{\varepsilon'_{r_{yy}} \cos^2(\theta)}{2n_y^4} + \frac{\varepsilon'_{r_{zz}} \sin^2(\theta)}{2n_z^4} - \frac{\varepsilon'_{r_{yz}} \sin(\theta)\cos(\theta)}{n_y^2 n_z^2} \right]$$

$$n'^{o}_{xz}(\theta) = \frac{\varepsilon'_{r_{yy}}}{2n_y} \quad \text{and} \quad n'^{e}_{xz}(\theta) = n^{e}_{xz}(\theta)^3 \times \left[\frac{\varepsilon'_{r_{xx}} \cos^2(\theta)}{2n_x^4} + \frac{\varepsilon'_{r_{zz}} \sin^2(\theta)}{2n_z^4} - \frac{\varepsilon'_{r_{xz}} \sin(\theta)\cos(\theta)}{n_x^2 n_z^2} \right] \tag{15}$$

Equations (15) provide the more general expressions including the three possible relationships between the symmetry elements and the dielectric frame, where the *x*-, *y*- or *z*-axes can be perpendicular to the mirror *m* or parallel to the two-fold axis *2*. Then $\varepsilon'_{r_{xy}} = \varepsilon'_{r_{xz}} = 0$ in the case of the *x*-axis; $\varepsilon'_{r_{xy}} = \varepsilon'_{r_{yz}} = 0$ in the case of the *y*-axis; $\varepsilon'_{r_{yz}} = \varepsilon'_{r_{xz}} = 0$ in the case of the *z*-axis.

The calculation of the sections of the imaginary index surface in the three principal planes of the dielectric frame from Eq. (15) allows us to clearly establish the comparison between the real and imaginary index surfaces. In both cases the ordinary angular distributions in the *xz* and *yz* planes, and the extraordinary distribution in the *xy* plane, are described by a circle. But there are several main strong differences: firstly the extraordinary sections in the *xz* and *yz* planes, and the ordinary section of the *xy* plane, are not ellipsoids but exhibit a bi-lobar shape; secondly there are umbilici not only in the *xz* plane, but also out of this plane, as further detailed in section 5; and finally the small and big axes of the bi-lobar patterns in the different principal planes are not the axes of the dielectric frame but the imaginary ones defined in section 2.2. In the case where the *y*-axis is perpendicular to the mirror *m* or parallel to the two-fold axis *2*, then the *y'*-axis corresponds to the *y*-axis, while the *x'*- and *z'*-axes are tilted from the *x*- and *z*-axes respectively by the angle $\theta_{\varepsilon'_r}$ expressed as:

$$\theta_{\varepsilon'_r} = \operatorname{atan}\left[\frac{\varepsilon'_{r_{xz}}}{\frac{1}{2}\left(\varepsilon'_{r_{zz}} - \varepsilon'_{r_{xx}}\right) + \left[\frac{1}{2}\left(\varepsilon'_{r_{zz}} - \varepsilon'_{r_{xx}}\right)^2 + \left(\varepsilon'_{r_{xz}}\right)^2\right]^{1/2}} \right] \tag{16}$$

For the two other conventions of relative orientation of the symmetry elements and the dielectric frame, $\varepsilon'_{r_{xz}}$, $\varepsilon'_{r_{zz}}$, and $\varepsilon'_{r_{xx}}$ in Eq. (16) have to be replaced term-to-term by $\varepsilon'_{r_{yz}}$, $\varepsilon'_{r_{zz}}$, and $\varepsilon'_{r_{yy}}$ when *x*-axis (along the *x'*-axis) is perpendicular to the mirror *m* or parallel to the two-fold axis *2*, and by $\varepsilon'_{r_{xy}}$, $\varepsilon'_{r_{xx}}$ and $\varepsilon'_{r_{yy}}$ when *z*-axis (along the *z'*-axis) is perpendicular to the mirror *m* or parallel to the two-fold axis *2*. Note that $\theta_{\varepsilon'_r}$ may vary as a function of the circular frequency or any dispersion parameter of the imaginary part of the relative dielectric permittivity.

Figure 2 give the angular distribution of the imaginary optical index in the *xz* and *yz* planes and in one fourth of the space respectively in the case of a monoclinic crystal where the *y*-axis is perpendicular to the mirror *m* or parallel to the two-fold axis *2*. The full analytical resolution of the absorption double-layer surface for monoclinic crystals has been done even without referring to the weak absorption hypothesis, which is complementary to the present review presentation [10, 11].

3.4. Symmetry analysis

In a similar approach to that of Neumann principle and Curie laws [1, 25, 26], the symmetry group of the angular distribution of the dielectric permittivity, $G_{\overline{\overline{\varepsilon}}_r}$, is given by the intersection of the symmetry groups of the real and

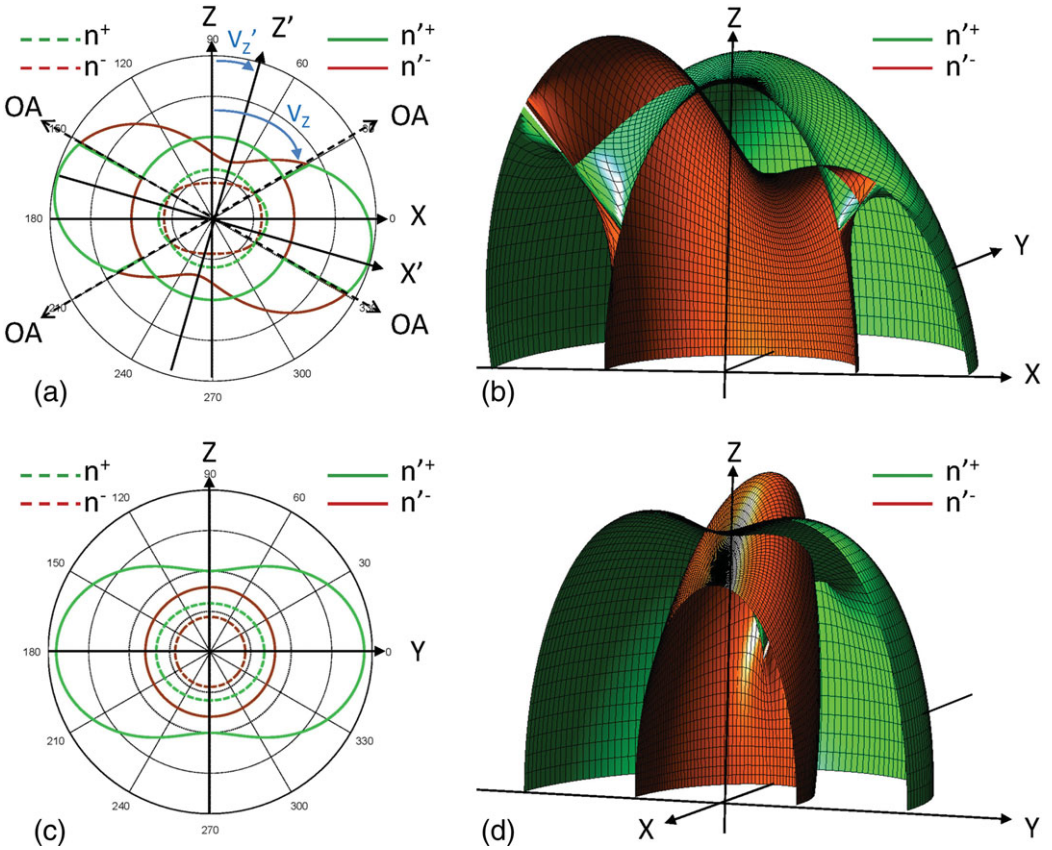

Figure 2 (online color at: www.lpr-journal.org) Imaginary index surface of a monoclinic crystal where the *y*-axis is perpendicular to the mirror *m* or parallel to the two-fold axis *2*; the superscripts (+) and (–) refer to the eigen polarization modes $\vec{e}^{+}$ and $\vec{e}^{-}$ respectively. (a) Section in the principal plane *xz* of the dielectric frame (*x*, *y*, *z*); the index surface at the center is drawn for reminding; n^{+} and n^{-} denote the external and internal layers of the index surface respectively and n'^{+} and n'^{-} are the corresponding imaginary layers; OA denotes the optical axes of internal conical refraction; (*x*′, *y*′, *z*′) is the principal frame of the imaginary index surface. (b) Schematic view from the *y*-axis in one fourth of the space. (c) Section in the principal plane *yz*; the index surface section is reminded at the center of the graph. (d) Schematic view from the *x* axis in one fourth of the space.

imaginary parts, $G_{\overline{\overline{\varepsilon_r}}}$ and $G_{\overline{\overline{\varepsilon'_r}}}$ respectively, i.e.:

$$G_{\overline{\overline{\hat{\varepsilon}_r}}} = \left(G_{\overline{\overline{\varepsilon_r}}} \cap G_{\overline{\overline{\varepsilon'_r}}}\right) \tag{17}$$

Each principal plane of each eigen frame acts as a symmetry mirror plane, so that the real and imaginary angular distributions should independently belong to the following orthorhombic point group: $G_{\overline{\overline{\varepsilon_r}}} = m_x m_y m_z$ and $G_{\overline{\overline{\varepsilon'_r}}} = m_{x'} m_{y'} m_{z'}$ where the notation m_q stands for the mirror symmetry related to the principal plane perpendicular to the given principal axis q in the related principal frame. Then according to Eq. (17), $G_{\overline{\overline{\hat{\varepsilon}_r}}} = \{m_x m_y m_z\} \cap \{m_{x'} m_{y'} m_{z'}\} = m_{y=y'}$, which is a monoclinic point group and highlights the fact that the dielectric and imaginary frames only share the axes $y = y'$ when one considers the case of a monoclinic crystal where the *y*-axis is perpendicular to the mirror *m* or parallel to the two-fold axis *2*. The same comments can be applied to the two other possibilities of relative orientation between the crystallographic symmetry operators and the dielectric frame.

In the weak absorption or fluorescence approximation, the imaginary part $\overline{\overline{\varepsilon'_r}}$ is much weaker than its real counterpart $\overline{\overline{\varepsilon_r}}$ so that the refractive index distributions are not affected by $\overline{\overline{\varepsilon'_r}}$ but are almost exclusively driven by $\overline{\overline{\varepsilon_r}}$. As a consequence, the symmetry group related to $n^{\pm}(\theta, \varphi)$ is directly $G_{\overline{\overline{\varepsilon_r}}} = m_x m_y m_z$ in the dielectric frame. As shown in Eq. (15), the imaginary angular distribution depends on both the imaginary part $\overline{\overline{\varepsilon'_r}}$ and real part $\overline{\overline{\varepsilon_r}}$, so that its symmetry group is $G_{\overline{\overline{\varepsilon'_r}}} = m_{y=y'}$ in the case where the *y*-axis is perpendicular to the mirror *m* or parallel the two-fold axis *2*. However, note that the pattern in Fig. 2(b) seems to have the *x*′*y*′ and *y*′*z*′ planes acting as mirror symmetry planes, which is contradictory to the symmetry group $G_{\overline{\overline{\varepsilon'_r}}} = m_{y=y'}$ that is found according to the group theory. In fact, the relative anisotropy of the real part defined as $(\varepsilon_{r_{zz}} - \varepsilon_{r_{xx}})\varepsilon^{-1}_{r_{yy}}$ is typically of the order of 10%, while it is rather 100% for the imaginary contribution $(\varepsilon'_{r_{zz}} - \varepsilon'_{r_{xx}})(\varepsilon'_{r_{yy}})^{-1}$ [13–15]. Thus there is more than one order of magnitude between the relative anisotropies of the real and imaginary contributions. It implies that in Eq. (15), the relative anisotropy

$n'^{e}_{xz}(\theta)$ is almost insensible to that of the refractive index contribution, especially the $n^{e}_{xz}(\theta)^3$ term. In such a situation, the symmetry group of $\overline{\overline{\varepsilon_r}}$ can be approximated to the identity symmetry group, that is to say the symmetry group of the sphere, i.e. $G_{\overline{\overline{\varepsilon_r}}} \cong G_{sphere}$. That means that the apparent symmetry group of the imaginary optical surface appears to be $G_{\overline{\overline{\varepsilon_r}}} = G_{sphere} \cap G_{\overline{\overline{\varepsilon'_r}}} = G_{\overline{\overline{\varepsilon'_r}}} = m_{x'}m_{y'}m_{z'}$, as observed in Fig. 2(b).

4. Measurement of real and imaginary optical index angular distributions

4.1. Dielectric frame orientation and principal refractive indices

As already discussed in section 3.2, the crystallographic and dielectric frames of a monoclinic crystal have only one axis in common: for example *b* (along the *2* axis) and *y* in BiB_3O_6 (crystal class *2*) [9], *b* (perpendicular to the mirror plane *m*), and *y* in $YCa_4O(BO_3)_3$ [YCOB] or Nd^{3+}:$YCa_4O(BO_3)_3$ [Nd:YCOB] (crystal class *m*) [27,28] and $Sn_2P_2S_6$ (crystal class *m*) [29]; *b* (along the *2* axis) and *x* in $KLu(WO_4)_2$ (crystal class 2/m) [30], and *b* (perpendicular to the mirror plane *m*) and *x* in $BaGa_4Se_7$ (crystal class *m*) [31]. Thus there is a degree of freedom in any monoclinic crystal where the dielectric frame may rotate around the common axis as a function of any dispersive parameter of the refractice index as the wavelength for example. The measurement of the angular range of this rotation has been determined in $Sn_2P_2S_6$ from the recording of transmission between two crossed polarizers trough slabs with their input and output faces perpendicular to the incident beam and to the *b*-axis simultaneously: a rotation of 9.6° was found when the wavelength varies from 0.6328 μm to 2 μm [29]. Up to 4° between 0.4 μm and 1 μm was reported for BiB_3O_6 by determining refractive indices from the measurement of the deviation angle in polarized light of a collinear light beam passing through prisms with their input faces normal to the incident light beam and to a crystallographic axis simultaneously. Then the rotation angle of the dielectric frame is calculated by considering the obtained values of refractive indices [9]. At the opposite, there is not such a rotation in the case of $YCa_4O(BO_3)_3$, Nd^{3+}:$YCa_4O(BO_3)_3$ and $KLu(WO_4)_2$ [27–29].

The orientation of the dielectric frame can be also easily determined by measuring the orientation of the neutral lines, i.e. $\vec{e}^{+}$ and $\vec{e}^{-}$ defined in section 3.1, associated with a light propagation along the common axis between the crystallographic and dielectric frame [9]: a slab of the studied crystal is placed between two cross polarizers, these two directions corresponding to the two orientations for which a total exctinction occurs. Below is described a method that is self-constent for the measurement of both the real and imaginary parts of the dielectric permittivity. This technique is based on a single sample shaped as a millimetric sphere polished to optical quality (see Fig. 3(a)). The spherical geometry is very interesting because it allows the light to propagate in any direction of the sample parallely to a diameter by keeping normal incidence. This method had been initially developped in the framework of nonlinear optics for the measurement of the phase-matching directions [32]. The sphere is stuck on a goniometric head under orientation using an X-rays automatic diffractometer. The measurement of the dielectric frame requires to stick the sphere along the common axis between the crystallographic and dielectric frames, and to propagate the light perpendicularly to this axis. An X-rays automatic diffractometer is coupled with a He-Ne laser beam focused in the sphere. Then from X-rays orientation it is possible to mark out the position of crystallographic axes, and if the common axis is *y* the laser beam enables the observation of the four hollow cones corresponding by pairs to the two optical axes of internal conical refraction [23]. The position of the principal axes of the dielectric frame are then easily and accurately determined since they are symmetrical in comparison with the OA of the dielectric frame as shown in Fig. 3(b) in the case of Nd:YCOB [28]. By coupling the sphere to a tunable laser source, it was shown in the case of Nd:YCOB that the relative orientation between the crystallographic and dielectric frames does not vary as a function of wavelength over the transparency range of the crystal within the accuracy of the experiments [28]. The classical method implemented to determine the three main refractive indices of biaxial crystals is based on the minimum deviation technique in two equilateral oriented prisms, a polarized tunable light allowing this measurement to be performed as a function of wavelength [33]. However for monoclinic crystals, due to the rotation of the dielectric frame, prims are usually cut with their input face normal to the incident light beam and to a crystallographic axis. Then one prism is cut with its input face perpendicular to the common axis between the crystallographic and dielectric frames, which leads to the magnitudes of two of the three principal refractive indices. The magnitude of the third index then requires the cutting of a second prism with its input face perpendicular to an other crystallograhic axis. In this case, the refractive index that is determined from the deviation angle measurement can be a principal value. It can also be a combination of two of them, according to the orientation of the index surface in the crystallographic frame. In that case the interpolation of the data using Eqs. (13) or (14) is required taking into account the angle between the dielectric frame and the crystallographic frame [9,29]. The reader may also refer to classical reviews where detailed descriptions of different strategies including prism methods for the refractive index measurement of monoclinic crystals can be found [10]. Note that the accuracy of measurements directly depends on the size of the prisms, which is not specific to monoclinic crystals. Because it is difficult to cut a prism with plane surfaces when only millimeter sizes of materials are available, the accessible accuracy is of about 10^{-3}; it can reach 10^{-4} for centimeter sizes. Other methods are based on Fresnel reflexion coefficients measurements, and Pulfrich or Abbe refractometers

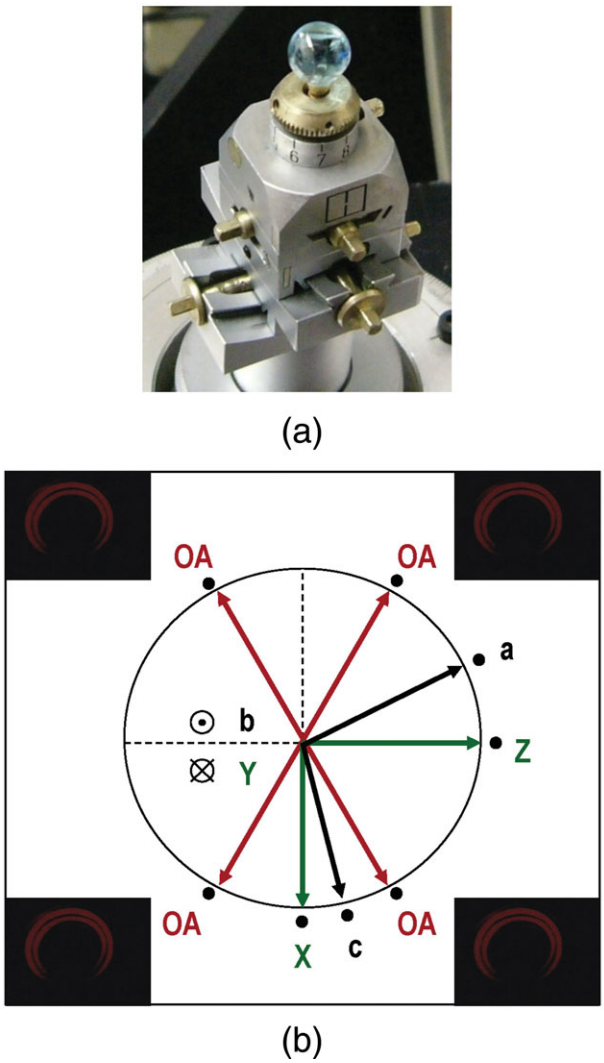

Figure 3 (online color at: www.lpr-journal.org) (a) Polished sphere of a Nd:YCOB crystal with a diameter of 7.44 mm. (b) Observation at the exit of the Nd:YCOB sphere of the four patterns of internal conical refraction using a HeNe beam at 632.8 nm that enables to determine the angles between the crystallographic frame (*a*, *b*, *c*) and the dielectric frame (*x*, *y*, *z*): (*a*, *z*) = 24.4 ± 0.5° and (*c*, *x*) = 13.4 ± 0.5°, with (*a*, *c*) = 101.0 ±0.2°.

with the same limitation as for the prism technique regarding the problem of possible dispersion of the orientation of the dielectric frame as a function of wavelength [34]. Contrary to all the above mentionned methods, the sphere method allows the three refractive indices to be easily measured as a function of the wavelength with an accuracy ranging between 10^{-3} and 10^{-4}. This technique relies on the measurement at each wavelength of the magnitude of the magnified spatial walk-off angle at the exit of the sphere as a function of the direction of propagation [35]. There is another possibility if the crystal exhibits nonlinear optical properties by simultaneously fitting the phase-matching curves measured at different wavelengths [30].

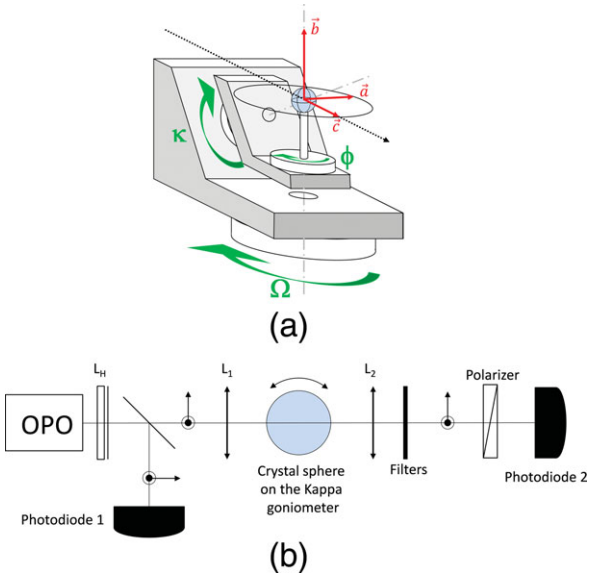

Figure 4 (online color at: www.lpr-journal.org) (a) Crystal sphere placed at the center of a Kappa goniometer. (b) Experimental setup for the direct measurement of the angular distribution of absorption or fluorescence of a crystal cut as a sphere; the arrows and dot circles denote the directions of the light polarization.

4.2. Absorption and fluorescence angular distributions and associated principal frames

Classically the spectra of absorption and fluorescence are recorded using polarized light propagating in slabs oriented along the principal axes of the dielectric frame and inserted in a spectrometer [36]. But as mentioned in section 3, the dielectric frame (x, y, z) does not correspond to the frame (x', y', z') of the imaginary part of the relative dielectric permittivity in general, so that the classical method does not lead to the principal values of the studied property in monoclinic crystals. It is why the sphere method has been proposed, the goal being to be able to perform direct measurements of the absorption and fluorescence spectra angular distributions with the crystallographic orientation of the studied crystal as the only prerequisite [13–15]. The demonstration of this technique for such a purpose was done for the study of Nd:YCOB. The oriented 7.44-mm-diameter Nd:YCOB sphere was placed at the center of an automatic Kappa circle as shown in Fig. 4(a), the three rotations ϕ, κ, Ω providing access of the full space with a precision better than 1 minute of Arc. The sphere was irradiated by a beam emitted by an optical parametric oscillator (OPO) tunable between 0.410 μm and 2.124 μm with a 10 Hz repetition rate and a pulse duration of 5 ns. The experimental setup is depicted in Fig. 4(b).

The absorption coefficient of Nd:YCOB was determined from the measurement of the transmission $T(\theta, \varphi)$ along each direction of propagation (θ, φ) inside the sphere corresponding to the ratio between the input laser power measured using the reference detector 1 and the output power from the sphere measured by detector 2 [13]. A filter

placed at the exit of the sphere allowed any possible fluorescence emission to be cut-off. The incident light was focused in the sphere by lens L1 so that it propagated under a parallel beam configuration inside the sphere [37]. A half-wave plate L_H enabled to successively select the two polarization eigen-modes of the considered direction of propagation. The corresponding absorption coefficient angular distributions taking into account Fresnel losses $T_F(\theta, \varphi)$ at the entrance and exit of the sphere were then determined from the following formula:

$$\alpha(\theta, \varphi) = -L^{-1} Ln[T(\theta, \varphi).T_F(\theta, \varphi)^{-1}] \qquad (18)$$

When dealing with fluorescence, a filter placed at the exit of the sphere cut the residual input beam and the power of fluorescence was recorded using detector 2 for the two polarization eigen-modes followed by the correction by Fresnel transmission relative to the exit of the sphere and the normalization by the incident pump power detected by detector 1. Figure 5(a) gives the angular distribution in the xz plane of the dielectric frame of the ordinary (o) and extraordinary (e) components of polarization of the absorption coefficient, $\alpha^o(\theta)$ and $\alpha^e(\theta)$ respectively, at 0.812 μm measured in a Nd:YCOB sphere. Figure 5(b) shows the angular distribution in the xz plane of the same Nd:YCOB sphere of the power emitted by fluorescence at 1.061 μm in the ordinary and extraordinary polarizations, $P^o(\theta)$ and $P^e(\theta)$ respectively; it has been normalized to the ordinary component of the fluorescence that is emitted along the z-axis, i.e. $P^o(\theta = 0)$.

Figure 5(a) shows that $\alpha^o(\theta)$ remains constant as a function of the direction of propagation θ while $\alpha^e(\theta)$ exhibits a bi-lobar angular distribution, which is in a very good accordance with the behaviour of the calculated patterns of Fig. 2(a) in the xz plane. Furthermore, Fig. 5(a) clearly indicates that the big and small axes of the extraordinary angular distribution, labelled as x'_{abs} and z'_{abs}, do not correspond to the axes x and z of the dielectric frame that are the symmetry axes of the extraordinary pattern of the index surface as shown in Fig. 1(a). There are also four directions along which the (o) and (e) absorption coefficients are equal. The same type of angular distribution was found for the fluorescence at 1.061 μm as shown in Fig. 5(b): the angular distribution of the ordinary component is described by a circle and that of the extraordinary one is a bi-lobar pattern. As for absorption, it was necessary to define specific principal axes for the extraordinary layer, i.e. x'_{fluo} and z'_{fluo}, that are different than x and z; but note that they are also different than x'_{abs} and z'_{abs}. The absorption and fluorescence experimental data were fitted using Eqs. (15) where the absorption coefficient and the normalized fluorescence power are related to the imaginary index n' by Eq. (10), the fitting parameters being $\varepsilon'_{r_{xx}}$, $\varepsilon'_{r_{yy}}$, $\varepsilon'_{r_{zz}}$ and $\varepsilon'_{r_{xz}} = \varepsilon'_{r_{zx}}$ according to Eq. (15). The corresponding fitting adjustments shown in Fig. 5(a) and (b) reveal the very good agreement between the model and the experiment. By inserting in Eq. (16) the fitting parameters that were previously found, it was possible to determine the tilt angle between the

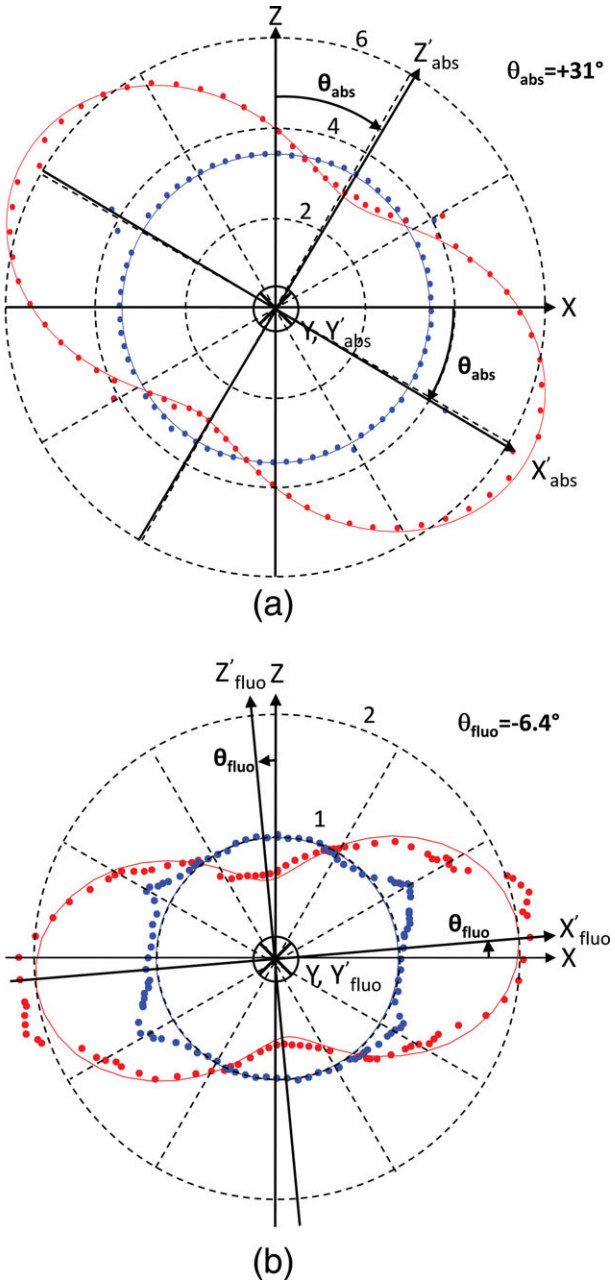

Figure 5 (online color at: www.lpr-journal.org) (a) Angular distribution of the absorption coefficient measured in the *xz* plane of a 7.44-mm-diameter Nd:YCOB sphere at 812 nm corresponding to the electronic transition of Nd^{3+} from the fundamental energy level $^4I_{9/2}$ to $^4F_{5/2} + {}^2H_{9/2}$. Concentric circles stand for absorption and it is in 2, 4 and 6 cm^{-1}. (b) Angular distribution of the power of fluorescence at 1.061 μm, corresponding to the electronic transition of Nd^{3+} from $^4F_{3/2}$ to $^4I_{11/2}$, normalized to the power of ordinary component of the fluorescence that is emitted along the *z*-axis when the Nd:YCOB sphere is pumped with the ordinary polarization component at 0.812 μm in the *xz* plane of the dielectric frame. The dots correspond to the measurement and the continuous lines to the fit according to Eq. (15). The blue color is for the ordinary (*o*) polarization of the light while the red is used for the extraordinary (*e*) polarization.

absorption frame (x'_{abs},y'_{abs}, z'_{abs}) and the dielectric frame (x, y, z), i.e. $\theta_{abs} = 31.1 \pm 0.7^\circ$ at 0.812 microns, and θ_{fluo} = -6.4 $\pm$ 0.9° at 1.061 microns between the fluorescence frame (x'_{fluo}, y'_{fluo}, z'_{fluo}) and the dielectric frame (x, y, z) [12]. The diagonalization of the matrix of absorption or fluorescence whose coefficients are the fitting parameters $\varepsilon'_{r_{xx}}$, $\varepsilon'_{r_{yy}}$, $\varepsilon'_{r_{zz}}$ and $\varepsilon'_{r_{xz}} = \varepsilon'_{r_{zx}}$ expressed in the dielectric frame leads to the determination of the magnitudes of the three principal coefficients of the imaginary dielectric permittivity $\varepsilon'_{r_{x'x'}}$, $\varepsilon'_{r_{y'y'}}$, $\varepsilon'_{r_{z'z'}}$ in the relevant imaginary frames. From these values, it is then easy to calculate the corresponding values of the absorption or fluorescence coefficients in their specific frames. In the case of the absorption for example, it gives: $\alpha_1 = 2.1 \pm 0.8$ cm^{-1}, $\alpha_2 = 3.5 \pm 0.4$ cm^{-1} and $\alpha_3 = 6.2 \pm 0.8$ cm^{-1} at 0.812 microns, where the indices 1, 2 and 3 refer to x'_{abs}, y'_{abs} and z'_{abs} respectively. These values are significantly different than those that would come from measurements performed along the axes of the dielectric frame, i.e.: $\alpha_1 = 3.2 \pm 0.4$ cm^{-1}, $\alpha_2 = 3.5 \pm 0.4$ cm^{-1} and $\alpha_3 = 5.1 \pm 0.6$ cm^{-1}, where the indices 1, 2 and 3 correspond in that case to the dielectric axes x, y and z respectively [13]. As a significant consequence for monoclinic crystals, it will be necessary to reconsider all the values tabulated in Handbooks, since they had been systematically measured in the dielectric frame instead of the absorption or fluorescence frames. Such a revision is of prime importance for the optimal exploitation of the monoclinic potentialities and thus for the design of any optical device based on these crystals.

Note that it is possible to determine the absorption and fluorescence emission angular distributions in polarized light even if a sphere of the studied crystal is not available. Actually a slab can work since it is sufficient to perform the measurement in only two directions of propagation considering the four associated polarization eigen modes: one direction can be the common axis between the crystallographic and dielectric frames, the second one being taken in the perpendicular plane, but out of the dielectric axes. Another alternative is to use three directions of propagation in the plane perpendicular to the common axis, as it was done for the Nd:LCB crystal [38]. The non-diagonal element requires at least one measurement out of the dielectric axes in the plane perpendicular to the common axis, and this measurement has to be performed as far as possible from both the dielectric axes for metrology precision issues.

It is expected that the orientation of the principal frame of absorption or fluorescence varies as a function of the transition that is considered. This feature has been verified by the measurement of the angular distribution of the absorption coefficient in polarized light in the xz plane of the Nd:YCOB sphere corresponding to seven electronic transitions from the fundamental energy level $^4I_{9/2}$ that were selected from the transmission spectra shown in Fig. 6 [15].

As an example for comparison with Fig. 5(a) corresponding to the transition $^4I_{9/2} \rightarrow (^4F_{5/2} + {}^2H_{9/2})$ at 812 nm, Fig. 7 gives the angular distribution of the absorption coefficient relative to the electronic transition $^4I_{9/2} \rightarrow (^2G_{7/2} + {}^4G_{5/2})$ at 595 nm. This direct comparison well establishes

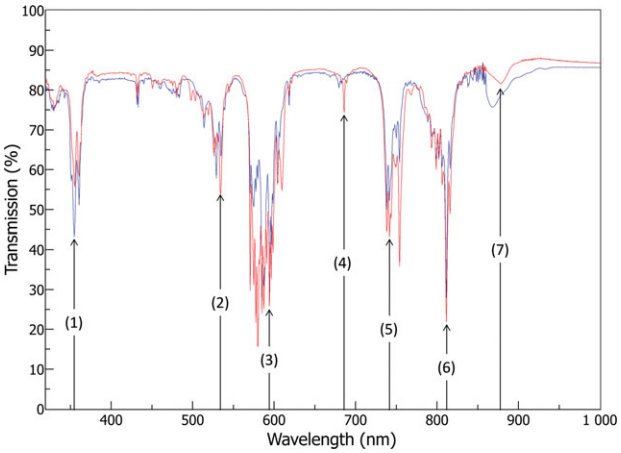

Figure 6 (online color at: www.lpr-journal.org) Transmission spectra of a Nd:YCOB slab cut along the z-axis of the dielectric frame, the light being polarized along the x-axis (red line) and the y-axis (blue line). The arrows indicate seven electronic transitions of the Nd^{3+} ion selected for the study for the angular distribution of the absorption coefficient from the $^4I_{9/2}$ fundamental energy level to ($^2I_{11/2} + {}^4D_{5/2}$) at 355 nm (1), $^2K_{13/2}$ at 534 nm (2), ($^2G_{7/2} + {}^4G_{5/2}$) at 595 nm (3), $^4F_{9/2}$ at 686 nm (4), $^4F_{7/2}$ at 742 nm (5), ($^4F_{5/2} + {}^2H_{9/2}$) at 812 nm (6), and to $^4F_{3/2}$ at 887 nm (7).

that the angle between the absorption frame and the dielectric frame strongly depends on the electronic transition, knowing that the dielectric frame orientation of Nd:YCOB does not depend on wavelength: $\theta_{abs} = 31^\circ$ at 0.812 μm, and $\theta_{abs} = -20^\circ$ at 0.595 μm.

Table 1 gives the angle θ_{abs} for the seven transitions that were considered, and it shows that the wavelength dependence of θ_{abs} is completely hieratic and does not follow a dispersion law.

The description of this phenomenon will require a microscopic quantum model taking into account the symmetry of the wave functions of the involved energy levels as well as the symmetry of the ions host crystallographic sites. It is an exciting challenge for further theoretical studies.

5. Absorption and fluorescence angular singularities and polarization specificities

5.1. Influence of the beam divergence in the vicinity of the optical axes

The refractive index surface is known to exhibit punctual discontinuities at the four umbilici directions, correlated to the $\pi/2$ polarization steps of the polarization vectors $\vec{e}^{\pm}(\theta, \varphi)$ [18, 23, 24]. As illustrated in Fig. 1, the index surface is characterized at the umbilici by first-order punctual discontinuities where the first-order angular derivative is no more defined. Absorption and fluorescence efficiencies are affected by the refractive index, as seen in Eq. (15). The refractive index angular distribution generally imposes to absorption and fluorescence a smooth and slowly-varying

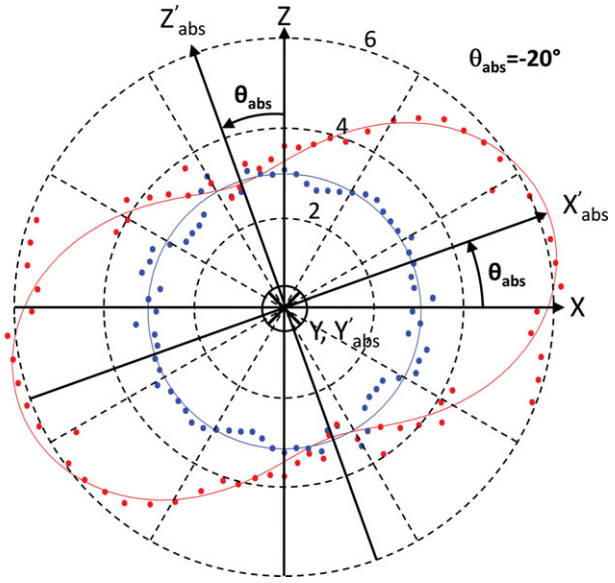

Figure 7 (online color at: www.lpr-journal.org) Angular distribution of the absorption coefficient measured in the *xz* plane of a 7.44-mm-diameter Nd:YCOB sphere at 595 nm corresponding to the electronic transition $^4I_{9/2} \rightarrow (^2G_{7/2} + {}^4G_{5/2})$ of Nd^{3+}. The dots correspond to the measurement and the continuous lines to the fit. The blue color is for the ordinary (*o*) polarization of the light while the red is used for the extraordinary (*e*) polarization.

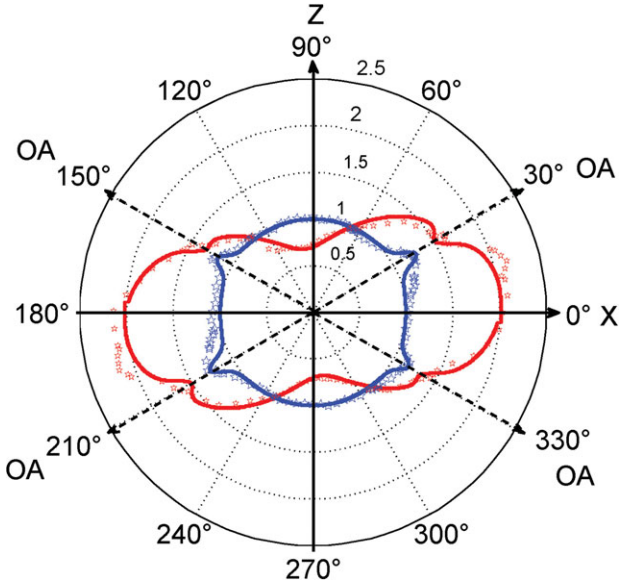

Figure 8 (online color at: www.lpr-journal.org) Angular distribution of the fluorescence corresponding to the transition $^4F_{3/2} \rightarrow {}^4I_{11/2}$ transition at 1061 nm in the *xz* plane of Nd:YCOB for the ordinary (blue) and extraordinary (red) polarizations. The dots correspond to the experimental data [13] and the continuous lines to the fit according to Eq. (19) [17].

Table 1 Measured rotation angle θ_{abs} between the dielectric frame (*x, y, z*) and the absorption frame (x'_{abs}, y'_{abs}, z'_{abs}) corresponding to seven electronic transitions of Nd:YCOB from the fundamental energy level $^4I_{9/2}$.

Wavelength (nm)	Excited energy level	θ_{abs}
355	$^2I_{11/2} + {}^4D_{5/2}$	$-12 \pm 2^\circ$
534	$^2K_{13/2}$	$-28 \pm 5^\circ$
595	$^2G_{7/2} + {}^4G_{5/2}$	$-20 \pm 2^\circ$
686	$^4F_{9/2}$	$-30 \pm 5^\circ$
742	$^4F_{7/2}$	$-23 \pm 2^\circ$
812	$^4F_{5/2} + {}^2H_{9/2}$	$+31 \pm 2^\circ$
887	$^4F_{3/2}$	$-5 \pm 2^\circ$

angular dependence. However it can lead to strong angular distortions while considering propagation directions close enough to the umbilici directions as depicted in Fig. 5 where it is shown that the phenomenon is particularly significant in the case of fluorescence measurements in Nd:YCOB. Actually along these directions, the polarization-orientation discontinuities provide punctual step discontinuities associated with the jump from an imaginary layer to the other one, leading to zero-order discontinuities. For measurements of absorption and fluorescence, light beams exhibit a non-zero angular divergence, even if it is a residual one. Therefore, when the propagation is close enough to the umbilici directions, experimental results in polarized light correspond to polarization-projected and angular-averaged measurements along the (θ, φ) propagation direction. They are spanning over the $(\Delta\theta, \Delta\varphi)$ angular integration, for the selected polarization projection along the $\vec{p}$ direction that is the orientation of the selected polarization through the polarized detection system for fluorescence collection. In the case of spontaneous fluorescence emission, where the "natural" divergence is strong especially due to the collection setup, the fluorescence coefficient $\xi(\theta, \varphi; \Delta\theta, \Delta\varphi; \lambda)$ corresponding to the collected emission is thus given by the following expression according to Eq. (10) [17]:

$$\xi(\theta, \varphi; \Delta\theta, \Delta\varphi; \lambda)(2\omega)^{-1}c = n'_{\exp}(\theta, \varphi; \Delta\theta, \Delta\varphi; \lambda) = \frac{\iint_{\Delta\theta,\Delta\varphi} n'^{+}(\theta', \varphi'; \lambda)[\vec{e}^{+}(\theta', \varphi').\vec{p}]^2 \sin(\theta')\, d\theta' d\varphi'}{\iint_{\Delta\theta,\Delta\varphi} \sin(\theta')\, d\theta' d\varphi'} + \frac{\iint_{\Delta\theta,\Delta\varphi} n'^{-}(\theta', \varphi'; \lambda)[\vec{e}^{-}(\theta', \varphi').\vec{p}]^2 \sin(\theta')\, d\theta' d\varphi'}{\iint_{\Delta\theta,\Delta\varphi} \sin(\theta')\, d\theta' d\varphi'} \quad (19)$$

Using Eq. (19) instead of Eq. (15) for the fit of the experimental data of fluorescence related to the $^4F_{3/2} \rightarrow {}^4I_{11/2}$ electronic transition in Nd:YCOB at 1061 nm provides a much better agreement in the vicinity of the optical axes, as shown in Fig. 8 compared with Fig. 5(b).

The model adjustment considered the angular integration over $\Delta\theta = 3^\circ$ and $\Delta\varphi = 7^\circ$, which is in good

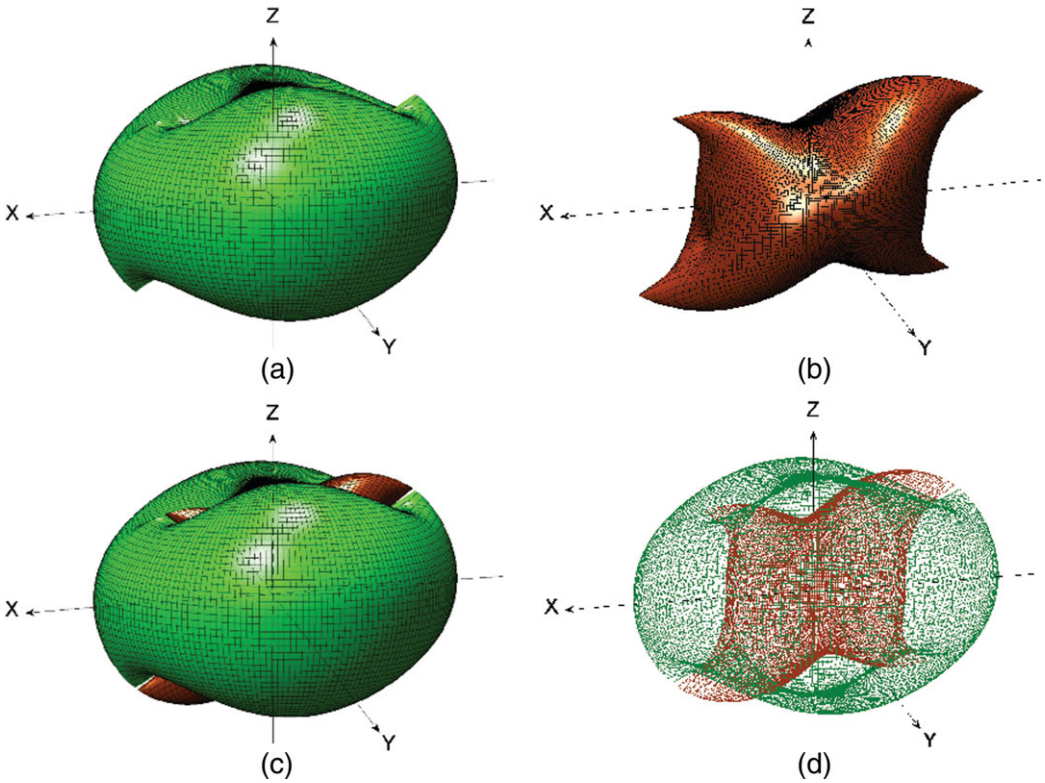

Figure 9 (online color at: www.lpr-journal.org) Calculated angular distribution of the fluorescence corresponding to the transition $^4F_{3/2} \rightarrow {}^4I_{11/2}$ at 1061 nm in Nd:YCOB. (a) and (b) correspond to the fluorescence layers associated with the external and internal layers of the index surface, respectively; (c) or (d) are the combinations of (a) and (b).

agreement with the experimental collection resolution of 7°. The $(\Delta\theta, \Delta\varphi)$ asymmetry can be related to the anisotropy asymmetry with the (θ, φ) angular coordinates, as well as to the experimental pumping asymmetry with an astigmatic incident beam [17].

Figure 9 gives the fluorescence full angular distributions calculated from the fitting parameters corresponding to the angular distribution measured in the *xz* plane of Nd:YCOB. These theoretical considerations bring significant consequences from a metrological point of view. One should perform experiments by considering beams with a divergence as small as possible for both absorption and fluorescence processes. The angular resolution of the collection setup, especially for spontaneous fluorescence emission, should be limited to prevent largely biased measurements resulting from undesired angular averaging. As seen in Fig. 8, experimental measurements along the umbilici directions would have led up to a 20% overestimation of the fluorescence cross-section corresponding to the ordinary polarization. Measurements should thus be performed far enough from these topological singularities, or with appropriate divergences, in order to ensure that the collected solid angle does not integrate strongly angular-varying directions.

Note that monoclinic non centro-symmetric crystals (point group m or 2) can also show optical activity, particularly in cases where the gyration tensor has a significant component for directions of optical axes of wave normal. Therefore in such cases, theoretical predictions that would only take into consideration the absorption, could deviate significantly from the experimental results in the vicinity of the optical axes, as it is the case for the real part of the index surface [39].

5.2. Directions of polarization insensitivity

As shown in Figs. 2(a) and (5), the imaginary layers intersect themselves in the *xz* principal plane. Such directions do not correspond to any discontinuity since they differ from the umbilici directions of the index surface. These directions thus correspond to polarization-independent directions for absorption or fluorescence: the magnitude of the considered property does not depend on the direction of polarization of light leading to an isotropic behavior. Moreover, such polarization-independent directions expand out of this principal plane, leading to the existence of a continuum of directions that verify $n'^{+}(\theta, \varphi) = n'^{-}(\theta, \varphi)$ as shown in Fig. 2(b). Note that this feature is not specific to monoclinic crystals, but it exists for any other biaxial crystal class [16]. It was partially experimentally reported for the first time by studying the $^4I_{9/2} \rightarrow ({}^4F_{5/2} + {}^2H_{9/2})$ absorption transition at 812 nm in Nd:YCOB as shown in Fig. 10 [14], and its full experimental report remains challenging [16].

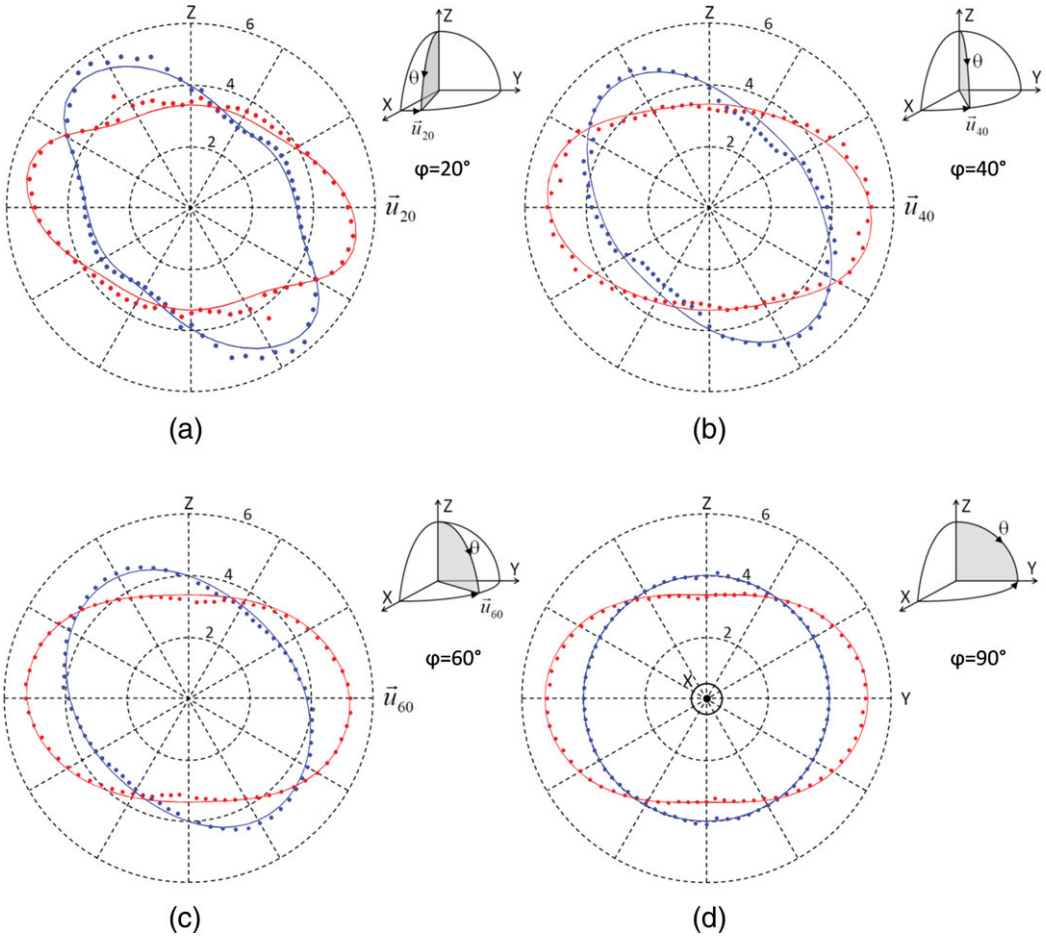

Figure 10 (online color at: www.lpr-journal.org) Angular distribution of the absorption coefficients $\alpha^{+}(\theta,\varphi)$ (blue) and $\alpha^{-}(\theta,\varphi)$ (red) in the dielectric frame (*x, y, z*) as a function of θ at $\varphi = 20^{\circ}$ (a), at $\varphi = 40^{\circ}$ (b), at $\varphi = 60^{\circ}$ (c) and at $\varphi = 90^{\circ}$ (d), angles relative to the two polarization modes (+) and (-) at 812 nm in Nd:YCOB. The dots correspond to the measurements and the continuous lines to the calculation. The concentric circles stand for the polar scale in 2, 4 and 6 cm^{-1}.

These polarization-insensitive directions correspond to the boundaries of specific angular zones that undergo layer inversion. Such layer-inversion zones correspond to spherical angles where the imaginary index surface undergoes the following unexpected relation of order $n'^{+}(\theta,\varphi) < n'^{-}(\theta,\varphi)$ while the refractive index surface undergoes $n^{+}(\theta,\varphi) > n^{-}(\theta,\varphi)$ by definition. Elsewhere, optical properties are associated with the following relations of order: $n'^{+}(\theta,\varphi) > n'^{-}(\theta,\varphi)$, while $n^{+}(\theta,\varphi) > n^{-}(\theta,\varphi)$. The consideration of these layer-inversion zones indicates that the strongest or weakest magnitude of the imaginary index is not systematically associated to the external, or internal refractive index layer. In other words, depending of the considered direction of propagation in the crystal, the experimental selection of the relevant polarization mode in order to optimize a given optical property is absolutely not trivial. Such optimization requires a great care from the experimental and theoretical points of view. Finally, the polarization-independent directions might further be considered for unpolarized beam, as well as to potentially minimize the mechanical stress related to thermal load [40].

6. Further open research fields on monoclinic crystal optics

6.1. Lasers

The preliminary characterization step for monoclinic laser crystals is the determination of the orientation of the dielectric frame [9,27,41], as well as those of the absorption and emission frames at each involved wavelength and temperature [13–15]. In the case of single-doped crystals, the absorption and fluorescence measurements need to be separately performed in each related eigen frame, taking into account the potential influence of the doping on the crystal matrix properties [28, 30]. Monoclinic crystals require extra-care when calculating a fluorescence lifetime with the Judd-Ofelt method by using the Füchtbauer-Ladenburg equation [30], and when exploiting the McCumber expression [42]. Additionally, the commonly-used reciprocity method should be considered in polarized light for four distinct absorption measurements that are necessary for the

determination of the four unknown tensor elements of the imaginary part of the relative dielectric permittivity [43]. However, when the calculated fluorescence properties are expressed in the frame where absorption properties had been previously measured, it is then required to convert these values in the fluorescence frame in order to obtain the principal emission cross-sections. In the case of multi-doped crystals, the spectroscopy of each optically active ion should be considered, both in absorption and emission. In the usual case of energy transfers, as it is the case between Yb^{3+} and Eu^{3+} for infrared laser telecom applications at 1.5 μm [44–46], the determination of the overall behaviour requires to study both angular distributions of the Yb^{3+} absorption and the Eu^{3+} emission, the net transfer process being statistically angulary averaged. Energy transfer related to charge transfer absorption and possible subsequent charge transfer emission should also be considered in the angular distribution approach in polarized light [47].

Figures of merit are often proposed to compare laser crystal candidates [48]. Such descriptions of laser potentiality should be displayed in polarized response, i.e. in the eigen modes (+) and (-), under optimal orientation. This orientation has to lead to the best compromise between the absorption and stimulated emission efficiencies taking into account the corresponding angular distribution. Scaling the output power of high-power laser systems, as diode-pumped solid state lasers for example, requires taking into account the thermal lens and thermally-induced radial birefringence. These thermo-optics effects, which strongly vary under non-lasing as well as lasing operation [49], generally tend to degrade high-power laser operation leading to front phase distortions, astigmatism and up to crystal cracking due to extreme temperature gradients [9, 45, 49, 50]. As for the real and imaginary parts of the dielectric permittivity, the anisotropies of the thermal expansion and thermal conductivity are described by second-rank polar symmetrical tensors, with four independent elements when written in the dielectric frame. The related principal frames, i.e. the expansion frame and the conductivity frame, also share a common axis, letting these frames free to rotate around this axis [8, 30, 45]. For optimal high-power lasing emission, the compromise for crystal orientation needs to balance both thermal expansion and conductivity with absorption and emission properties, these properties showing generally principal values in distinct directions. Such optimization can also include tailored pump transverse profiles and polarizations [9]. In particular, there are distinct directions where the optical path appears to be insensitive to temperature changes [50]. In this framework, thin-disk geometries offer a very interesting configuration to cope and prevent thermal effects for high-power laser devices. As for bulk devices, angular distributions require to properly define the optimal crystal orientation. In the case of composite materials with a doped laser layer deposed on a non-doped substrate, an additional constraint to the optimal orientation relies of the minimization of the lattice mismatch between the two materials as reported in Tm:$KLu(WO_4)_2$/$KLu(WO_4)_2$ [2], showing that mechanical constraints have to be considered in addition to optical properties as refractive index differences [31], or epitaxial growth rates for the oriented active layers [51]. In the femtosecond regime, there are additional constraints, since ultrashort pulses are sustained by a large spectrum [52, 53], which implies a large range of orientations of the different optical frames. The optimal "time bandwidth" product should be then explored out of the typical directions of propagation [30].

6.2. Laser and nonlinear frequency conversion in the same crystal

The calculation of the phase-matching directions of nonlinear sum- and difference-frequency generations corresponding to the different configurations of polarization [54] requires the usual precaution to consider the index surface at each involved wavelength in its associated dielectric frame, especially in the case of monoclinic nonlinear crystals where the dielectric frame may exhibit a significant dispersion of orientation with wavelength [9]. When dealing with self-frequency properties, i.e. in laser crystals that have nonlinear frequency conversion properties too, the definition of the optimal direction becomes more complicated [4, 55–58]. Actually absorption, laser emission and nonlinear properties should be optimal in three distinct frames, so that self-frequency conversion, as for example the self-frequency doubling of the laser emission, is no longer equivalent along the 8 phase-matching directions that are equivalent from the nonlinear point of view in the dielectric frame [4, 13]. Moreover, the full evaluation of the potentiality of a self-frequency material should also consider excitation state absorption (ESA) at both the laser and the frequency-doubled wavelengths, which might show distinct excited state absorption frames since distinct ESA transitions would be solicited. Note that the formalism that we described above can be applied to ESA, which needs to replace former attempts of angular distributions [59]. Absorption and Raman spectra also show polarization and orientation dependence in monoclinic doped or co-doped crystals [61–63]. The principal directions for Raman emission are then also expected to be distinct to that of laser emission. Recently, laser emission [63] and Raman gain [64] have been independently reported in laser-written waveguides in Yb:$KGd(WO_4)_2$. The next breakthrough for such integrated telecom devices should thus come from the simultaneous optimization of the laser emission and Raman amplification. In the same framework, it is also important to check the guiding efficiency as a function of the direction of propagation from the confinement point of view: different magnitudes of laser emission power were reported in Yb:KGW and Yb:KYW [60], as well as distinct Raman gains in KGdW [64]. In such wave-guided configurations, the optimization of polarization-dependent angular distributions of laser properties might also consider the competition between the guiding behavior and the off-axis energy propagation due to spatial walk-off.

6.3. Scintillators

Scintillation offers large capabilities and applications, spanning from neutron detection in medical imaging to the foreseen detection of solar neutrinos in fundamental physics. The determination of the potential of promising monoclinic crystals for scintillation detectors, as example Pb^{2+}:$YCa_4O(BO_3)_3$ [5], Pr^{3+}:$Lu(SiO_4)O$ [65], Yb^{3+}:$LiY_6O_5(BO_3)_3$ [47], or Ce^{3+}:$Lu(SiO_4)O$ [66], includes various types of irradiations as α-rays, neutrons, UV, or even γ-rays and X-rays irradiations [5, 47, 65], as well as photoconductivity [66]. Such irradiations provide the optical fluorescence-induced response in the spectral domain as well as in the time domain. The knowledge of the neutron absorption anisotropy is out of the scope of this paper, since it is related to an interaction with the nucleus. However, it looks reasonable to consider that X-ray absorption might be anisotropic, following angular trends similar to those developed here. It is even clearer that UV irradiation, often used in UV-to-visible charge transfer emission to mimic particle irradiation [47], should provide angular distributions as described above, with distinct optimal directions and eigen frames for both the charge transfer excitation and the resulting charge transfer emission. Such studies with oriented crystals or spheres in polarized light should permit to successively determine the best conditions for the scintillation excitation and for the subsequent fluorescence emission. Evaluating the scintillation performances with oriented crystals in polarized light should also provide additional advantages. At first using the relevant orientations leading to an enhancement of the process, it is expected to be able to measure larger signals, which thus would increase the signal-to-noise ratio and gives access to better resolved scintillation parameters as kinetics behavior and lifetimes of fluorescent emitter levels [65]. Secondly, the inter-comparison of scintillation usually relies on neutron-to-photons or photon-per-MeV-α estimations with no mention about the studied crystal orientation nor the typical solid angles considered for both irradiation and collection. The reliability of such approach could be improved by giving truly intrinsic scintillation efficiency per material, so as to provide its best capabilities and to compare materials between each other for equivalent estimation conditions. Third, such studies should provide the resulting optimal compromise for the crystal orientation along directions out of the dielectric axes, for each targeted application, depending on whether only emission or both excitation and emission processes should have anisotropic behavior.

6.4. Beyond the linear imaginary dielectric response: multi-photon processes and two-photon excited fluorescence

Nowadays, very high peak powers and intensities can be reached with ultrafast lasers in the picosecond or femtosecond regimes, so that multi-photon processes can happen in crystals, even below optical damage threshold. Despite the weak nonlinear cross-sections, multi-photon absorption can occur by close-to-resonance enhancement of the nonlinear susceptibilities [67]. Such an enhancement especially happens in two-photon absorption process when the second harmonic of the fundamental wavelength tends to match the energy gap either from the crystal matrix band gap or from some discrete energy levels associated to laser active doping elements. Even if three-photon excited fluorescence had been reported in a non-doped crystal for domestic lightning issues [68], we focus hereafter on two-photon excited fluorescence that can show significant pump-polarization dependence and anisotropy. Two-Photon processes are nonlinear optical interactions that are governed by the third order dielectric permittivity [69]. The corresponding anisotropy is described by a four-rank polar tensor written as 3×27 matrix so that it has no meaning to talk about a "two-photon eigen frame" since neither its real nor imaginary parts can be written in a diagonal way. However with a direct analogy to the first order dielectric permittivity, it is expected that some additional elements shall be non-zero in the imaginary part with respect to those in the real part when expressed in the dielectric frame. It is an open question to know what elements shall switch on for monoclinic systems, depending on the considered point group. The demonstration of these new elements is thus challenging from a fundamental point of view, since they are necessary to properly describe the still-unknown angular distributions in polarized light of multi-photon absorption or emission processes. Such fundamental considerations should help for processing waveguides under the technique of laser writing such as in BiBO in order to achieve nonlinear frequency conversion [70], in KGW for Raman-gain amplification [64] or in Yb-doped KGW for laser emission [63]. Finally, it might also be considered in very high average power laser systems where nonlinear absorption may bring non-negligible additional laser material heating, to properly model and design the removal of the total thermal load.

6.5. Anisotropy of photorefractive response in monoclinic crystals

Another type of nonlinear optical wave mixing which is very strongly affected by the low symmetry of the crystal is based on photorefractive effect [6]. It occurs in crystals lacking the symmetry center, where the refractive index might change because of spatial redistribution of the light induced charge carriers and subsequent development of the static space-charge field. The resulting refractive index variation depends on optical as also on electrical and electrooptical properties, described, each, by its relevant tensor. With the rare exceptions, all known photorefractives belong to crystal systems with relatively high symmetry: cubic (class 23 for sillenites and class $\bar{4}3m$ for most semiconductor photorefractives), trigonal (class $3m$ for lithium niobate and lithium tantalate), tetragonal (class $4mm$ for barium titanate). Some promising photorefractive crystals belong however to crystal systems with lower symmetry,

orthorhombic (class $mm2$ for $BaNaNb0_3$ and $KNbO_3$) and monoclinic (class m for $Sn_2P_2S_6$). The last material is especially attractive because it combines a quite high nonlinear response with a short response time, and it is sensitive in the red and near infrared spectrum range [71]. The optimization of the beam coupling for this crystal is far from being trivial because of the mentioned difficulties, typical for work with low-symmetry materials. The optical frame in $Sn_2P_2S_6$ does not coincide with the conventional crystallographic frame in which the $\hat{y}$-axis is normal to the mirror plane: note that here we adopt the convention of the related reference articles [71–73], where $(\hat{x}, \hat{y}, \hat{z})$ stands for the considered crystallographic frame. The long axis of the index ellipsoid for the red wavelength of the He-Ne laser makes an angle $+43^o$ with respect to the crystallographic $\hat{x}$-axis at room temperature. The low frequency dielectric susceptibility surface is also tilted in the $\hat{x}\hat{y}$ plane to $\approx +14^o$. The angular dependences of the nonlinear coupling coefficients for $Sn_2P_2S_6$ have been calculated for three principal planes $\hat{x}\hat{y}$, $\hat{y}\hat{z}$ and $\hat{x}\hat{z}$ [72]. According to the results obtained, the largest coupling coefficients in $\hat{x}\hat{y}$-plane were expected for quite unusual orientations of the interacting waves, tilted roughly to 20^o with respect to the crystal $\hat{y}$-axis. The experimental measurements confirmed these expectations and demonstrated the increasing by a factor 2 of the coupling coefficient at optimized angle as compared with standard beams orientation along the crystal $\hat{x}$-axis. The low symmetry of $Sn_2P_2S_6$ manifests itself also in photorefractive beam fanning, which is a kind of frequency degenerate nonlinear scattering. As distinct from the fanning in the $\hat{x}$-cut or $\hat{y}$-cut $BaTiO_3$ or $LiNbO_3$, the fanning in $Sn_2P_2S_6$ is obviously spatially non uniform in polarization [73].

7. Conclusion

The considerations that are developed above show that monoclinic crystals exhibit non trivial and original optical features when compared with higher symmetry crystals, which may explain the fact that they had not been considered often in the past despite real potentialities. However the modelling and measurement methodologies that are reported here should help to characterize at best such low symmetry crystals and so help to promote and increase their use in optical devices based on lasers or incoherent light.

These comments are *a fortiori* relevant for triclinic crystals especially since they have the lowest symmetry, the two corresponding crystal classes being 1 and $\bar{1}$. These crystals belong also to the biaxial optical class and they will exhibit the same main features as those of monoclinic crystals with one more step of difficulty since there are no common axes between the frames of the real and imaginary parts of the dielectric permittivity and there are four more different non-diagonal elements in the corresponding tensors when expressed in the dielectric frame.

The next step in the modelling of the electro-magnetic anisotropy of monoclinic as well as triclinic crystals will be to develop the theory allowing these macroscopic properties to be linked with the microscopic ones in the framework of *ab initio* calculation. It will be then necessary to use a quantum model describing at best the potential energy of the valence electrons from the symmetry of the wave functions of the energy levels that are considered as well as the symmetry of the crystallographic sites that are involved. It is undoubtedly an exciting challenge.

Key words: Crystal optics, refractive indices, absorption, fluorescence, monoclinic crystals.

Yannick Petit received his PhD degree in 2007 at the University of Grenoble, France. After a post-doctoral position at the University of Geneva, he became Assistant Professor at the University of Bordeaux in 2010, where he joined the Institute of Chemistry and Condensed Matter of Bordeaux. He has investigated the anisotropy of linear and nonlinear optics properties in crystals, as well as femtosecond terawatt laser beam propagation for atmospheric applications. His current field of research deals with Direct Laser Writing in tailored materials and advanced microscopy.

Simon Joly received his PhD degree in 2009 at the University of Grenoble, France. After two postdoctoral positions, in Japan in 2010 at the Institute of Molecular Science then in 2011 in Chambery at the IMEP-LAHC laboratory, he joined the Commissariat à l'Energie Atomique in Grenoble. He has been involved in nonlinear optics, laser and terahertz spectroscopy research activities, he is now investigating Infrared Imaging technology applied to skin cancer detection.

Patricia Segonds received her PhD degree in 1989, and is now Professor at the University of Grenoble. From 1990 she joined the Centre de Physique Moléculaire et Optique Hertzienne from University of Bordeaux. Her research interest has been femtosecond lasers, pump probe techniques and nonlinear glasses for all optical switching. In 1998 she joined the Laboratoire de Spectrométrie Physique and since 2007 the Institut Néel of Grenoble. Her research field deals with the generation of parametric light in nonlinear crystals, and monoclinic crystals optics. She has authored 72 papers in refereed journals and conference proceedings.

Benoît Boulanger received his PhD degree in 1989 at the University of Nancy in France. Since 2000 he is Professor at the University of Grenoble where he joined the Laboratoire de Spectrométrie Physique and Institut Néel from 2007. In 2012 he became a Fellow of the Optical Society of America and of the European Optical Society. He will be general co-chair of the international conference "Non Linear Optics – 2013" in Hawaii. He has authored over 150 papers in refereed journals and conference proceedings on many aspects of crystal optics, including laser, nonlinear and quantum optics.

References

[1] A. Authier, International Tables for Crystallography Vol. D, Ed., International Union of Crystallography, (Kluwer Academic Publisher, Dordrecht, Netherlands, 2006), chap 1.1.

[2] S. Vatnik, I. Vedin, M. C. Pujol, X. Mateos, J. J. Carvajal, M. Aguilo, F. Díaz, U. Griebner, and V. Petrov, Laser Phys. Lett. **7**, 435–439 (2010).

[3] G. Aka, E. Reino, P. Loiseau, D. Vivien, B. Ferrand, L. Fulbert, D. Pelenc, G. Lucas-Leclin, and P. Georges, Opt. Mater. **26**, 431–436 (2004).

[4] P. Segonds, S. Joly, B. Boulanger, Y. Petit, B. Ménaert, and G. Aka, J. of Opt. Soc. Am. B. **26**, 750–753 (2009).

[5] Y. Fujimoto, T. Yanagida, Y. Yokota, N. Kawaguchi, K. Fukuda, D. Totsuka, K. Watanabe, A. Yamazaki, V. Chani, and A. Yoshikawa, Nucl. Instr. and Meth. In Phys. Research. A **652**, 238–241 (2011).

[6] Photorefractive materials and their applications, Vol. 1–3, P. Günter, and J.-P. Huignard, eds. (Springer-Verlag, Heidelberg, 2007).

[7] J. J. Longdell, E. Fraval, M. J. Sellars, and N. B. Manson, Phys. Rev. Lett. **95**, 063601–1-4 (2005).

[8] J. F. Nye. Physical Properties of Crystals: Their Representation by Tensors and Matrices (Oxford University, Oxford, 1985).

[9] H. Hellwig, J. Liebertz, and L. Bohaty, J. Appl. Phys. **88**, 240–244 (2000).

[10] G. Szivessy, Handbuch der Physik, Vol. 20, Ch. 11 (Julius Springer, Berlin, 1928).

[11] A. M. Goncharenko, Sov. Phys. Crystallography **4**, 365–370 (1960).

[12] Born & Wolf, Principles of Optics, (Pergamon Press, Oxford, 1965) chap. 14.

[13] Y. Petit, B. Boulanger, P. Segonds, C. Félix, B. Ménaert, J. Zaccaro, and G. Aka, Opt. Express **16**, 7997–8002 (2008).

[14] S. Joly, Y. Petit, B. Boulanger, P. Segonds, C. Félix, B. Ménaert, and G. Aka, Opt. Express **17**, 19868–19873 (2009).

[15] S. Joly, P. Segonds, B. Boulanger, Y. Petit, C. Félix, and B. Ménaert, Opt. Express **18**, 19169–19174 (2010).

[16] Y. Petit, P. Segonds, S. Joly, and B. Boulanger, Materials **3**, 2474–2482 (2010).

[17] Y. Petit, S. Joly, P. Segonds, and B. Boulanger, Laser Physics **21**, 1–8 (2011).

[18] A. Yariv, "Quantum Electronics", Second Edition, (Holt, Rinehart and Winston, Inc., New York, 1976).

[19] N. Ashcroft and N. D. Mermin, Solid State Physics, (Saunders College, Philadelphia, 1976).

[20] L. A. Shuvalov, Springler series in solid-state sciences **37**, (Springer Verlag, Heidelberg, 1981).

[21] B. Boulanger, and J. Zyss, in International Tables for Crystallography Vol. D: A. Authier Ed., (International Union of Crystallography, Kluwer Academic Publisher, Dordrecht, Netherlands, 2006), chap. 1.7

[22] J. Q. Yao and T. S. Fahlen, J. Appl Phys. **55**, 65–68 (1984).

[23] J. P. Fève, B. Boulanger, and G. Marnier, Optics Comm. **105**, 243–252 (1994).

[24] B. Boulanger and G. Marnier, Optics Comm. **72**, 144–147 (1989).

[25] Y. Petit, B. Boulanger, P. Segonds, and T. Taira, Phys. Rev. A **76**, 063817–1-7 (2007).

[26] A. V. Shubnikov and V. A. Koptsik, Symmetry in science and art (Plenum Press, New York, 1974).

[27] P. Segonds, B. Boulanger, J. P. Fève, B. Ménaert, J. Zaccaro, G. Aka, and D. Pelenc, J. Opt. Soc. Am. B **21**, 765–779 (2004).

[28] P. Segonds, B. Boulanger, B. Ménaert, J. Zaccaro, J. P. Salvestrini, M. D. Fontana, R. Moncorgé, F. Porée, G. Gadret, J. Mangin, A. Brenier, G. Boulon, G. Aka, and D. Pelenc, Opt. Mater. **29**, 975–982 (2007).

[29] D. Haertle, A. Guarino, J. Hajfler, G. Montemezzani, and P. Günter, Opt. Express **13**, 2047–2057 (2005).

[30] V. Petrov, M. C. Pujol, X. Mateo, O. Silvestre, S. Rivier, M. Aguilo, R. Maria Solé, J. Liu, and F. Diaz, Laser & Photon. Rev. **1**, 179–212 (2007).

[31] W. Bolaños, J. J. Carvajal, X. Mateos, E. Cantelar, G. Lifante, U. Griebner, V. Petrov, V. L. Panyutin, G. S. Murugan, J. S. Wilkinson, M. Aguiló, and F. Díaz, Opt. Express **19**, 1449–1454 (2011).

[32] G. Marnier and B. Boulanger, Optics Comm. **72**, 139–143 (1989).

[33] W. L. Bond, J. of Appl. Physics, **36**, 1674–1677 (1965).

[34] C. S. Hurlbu, Am. Mineralogist, **69**, 391–398 (1984).

[35] P. Segonds, B. Boulanger, L. Ferrier, B. Ménaert, and J. Zaccaro, J. Opt. Soc. Am. B **23**, 852–856 (2006).

[36] A. R. H. Cole, J. Opt. Soc. Am., **44**, 741–743 (1954).

[37] B. Boulanger, J. P. Fève, G. Marnier, C. Bonnin, P. Villeval, and J. J. Zondy, J. Opt. Soc. Am. B **14**, 1380–1386 (1997).

[38] A. Brenier, Y. Wu, J. Zhang, Y. Wu, and P. Fu, J. of Appl. Phys. **108**, 093101–1-5 (2010).

[39] W. Voigt, Ann. Phys. **18** 645 (1905).

[40] Landau & Lifchitz, Theory of Elasticity, (MIR Editions, Moscova, 1967).

[41] Q. Ye. and B. H. T. Chai, J. of Crystal Growth **197**, 228–235 (1999).

[42] D. E. McCumber, Phys. Rev. **136**, A954–A957 (1964).

[43] A. Brenier, Y. Wu, J. Zhang, and Y Wu, Appl. Physics B **107**, 59–65 (2012).

[44] P. A. Burns, J. M. Dawes, P. Dekker, J. A. Piper, H. Jiang, and J. Wang, IEEE J. Quantum Electron. **40**, 1575–1582 (2004).

[45] W. W. Ge, H. J. Zhang, J. Y. Wang, M. H. Jiang, S. Q. Sun, D. G. Ran, H. R. Xia, and R. I. Boughton, J. Appl. Cryst. **40**, 125–132 (2007).
[46] X. Mateos, R. Solé, J. Gavaldà, M. Aguiló, J. Massons, and F. Díaz, Opt. Mat. **28**, 423–431 (2006).
[47] J. Sablayrolles, V. Jubera, F. Guillen, and A. Garcia, Spectrochimica Acta Part A **69**, 1010–1019 (2007).
[48] R. Gaume, P. H. Haumesser, B. Viana, D. Vivien, B. Ferrand, and G. Aka, Opt. Mat. **19**, 81–88 (2002).
[49] S. Chénais, F. Druon, F. Balembois, G. Lucas-Leclin, Y. Fichot, P. Georges, R. Gaumé, B. Viana, G. P. Aka, and D. Vivien, Opt. Mat. **22**, 129–137 (2003).
[50] S. Biswal, S. P. O'Connor, and S. R. Bowman, Appl. Opt. **44**, 3093–3097 (2005).
[51] A. Aznar, R. Solé, M. Aguiló, F. Diaz, U. Griebner, R. Grunwald, and V. Petrov, Appl. Phys. Lett. **85**, 4313–4315 (2004).
[52] F. Druon, S. Chénais, F. Balembois, P. Georges, A. Brun, A. Courjaud, C. Hönninger, F. Salin, M. Zavelani-Rossi, F. Augé, J. P. Chambaret, A. Aron, F. Mougel, G. Aka, and D. Vivien, Opt. Mat. **19**, 73–80 (2002).
[53] M. Delaigue, V. Jubera, J. Sablayrolles, J.-P. Chaminade, A. Garcia, and I. Manek-Hönninger, Appl. Phys. B **87**, 693–696 (2007).
[54] J. P. Fève, B. Boulanger, and G. Marnier, Optics Comm. **99**, 284–302 (1993).
[55] J. M. Eichenholz, D. A. Hammons, L. Shah, Q. Ye, R. E. Peale, M. Richardson, and B. H. T. Chai, Appl. Phys. Lett. **74**, 1954–1956 (1999).
[56] L. Gheorghe, P. Loiseau, G. Aka, and V. Lupei, Opt. Mat. **30**, 44–46 (2007).
[57] G. Aka and A. Brenier, Opt. Mat. **22**, 89–94 (2003).
[58] F. Mougel, K. Dardenne, G. Aka, A. Kahn-Harari, and D. Vivien, J. Opt. Soc. Am. B **14**, 164 (1999).
[59] C. Maunier, J. L. Doualan, G. Aka, J. Landais, E. Antic-Fidancev, R. Moncorgé, and D. Vivien, Optics Comm. **184**, 209–214 (2000).
[60] V. Krishnakumar and R. Nagalakshmi, Spectrochimica Acta Part A **60**, 2733–2739 (2004).
[61] L. Macalik, J. Hanuza, and A. A. Kaminskii, Journal of Molecular Structure **555**, 289–297 (2000).
[62] G.-W. Lu, C.-X. Li, W.-C. Wang, Z.-H. Wang, H.-R. Xia, H.-J. Zhang, X.-L. Meng, and L.-X. Li, Chemical Physics Letters **368**, 269–275 (2003).
[63] F. M. Bain, A. A. Lagatsky, R. R. Thomson, N. D. Psaila, N. V. Kuleshov, A. K. Kar, W. Sibbett, and C. T. A. Brown, Opt. Express **17**, 22417–22422 (2009).
[64] S. M. Eaton, C. A. Merchant, R. Iyer, A. J. Zilkie, A. S. Helmy, J. S. Aitchison, P. R. Herman, D. Kraemer, R. J. D. Miller, C. Hnatovsky, and R. S. Taylor, Applied Physics Letters **92**, 081105–1-3 (2008).
[65] M. Nikl, H. Ogino, A. Beitlerova, A. Novoselov, and T. Fukuda, Chem. Phys. Lett. **410**, 218–221 (2005).
[66] M.-F. Joubert, S. A. Kazanskii, Y. Guyot, J.-C. Gâcon, and C. Pédrini, Phys. Rev. B **69**, 165217–1-13 (2004).
[67] R. W. Boyd, Nonlinear optics, Third Edition, (Academic Press ELSEVIER, San Diego, 2008).
[68] L. Yang, C. Wang, Y. Dong, N. Da, X. Hu, D. Chen, and J. Qiu, Opt. Express **13**, 10157–10162 (2005).
[69] J. A. Armstrong, N. Bloembergen, J. Ducuing, and P. Pershan, Phys. Rev. **127**, 1918–1939 (1962).
[70] S. J. Beecher, R. R. Thomson, D. T. Reid, N. D. Psaila, M. Ebrahim-Zadeh, and A. K. Kar, Opt. lett. **36**, 4548–4550 (2011).
[71] S. Odoulov, A. Shumelyuk, U. Hellwig, R. Rupp, A. Grabar, and I. Stoyka, J. Opt. Soc. Am. B **13**, 2352 (1996).
[72] A. Shumelyuk, A. Volkov, S. Odoulov, G. Cook, and D. R. Evans, Appl. Phys. B **100**, 101–108 (2010).
[73] A. Shumelyuk, A. Volkov, A. Selinger, M. Imlau, and S. Odoulov, Opt. Lett. **33**, 150–152 (2008).